Alma Mater Studiorum · Università di Bologna

School of Science
Department of Physics and Astronomy
Bachelor degree in Physics

Determination of the top-quark mass using top-antitop cross section measurements at LHC

Supervisor:
Prof. Mauro Villa

Co-supervisor:
Dr. Lorenzo Bellagamba

Submitted by:
Elena Cuppini

Academic Year 2020/2021

Abstract

The study of top-quark physics represents an active research field for the theoretical community and it is a part of high interest in the experimental physics program at ATLAS. In this thesis, the mass of the top-quark is extracted through the comparison of QCD calculations of the total and differential cross-sections of top-quark pair production in proton-proton collisions at a centre of mass energy of $\sqrt{s} = 13$ TeV, produced with the program MATRIX at next-to-next-to-leading order, with experimental data from pp collisions at $\sqrt{s} = 13$ TeV collected in 2015 and 2016 by the ATLAS detector at the CERN Large Hadron Collider (LHC), corresponding to an integrated luminosity of 36.1 fb^{-1}. Using measured top-antitop ($t\bar{t}$) total cross-section in $e\mu$ dilepton events and conducting an analysis based on a Bayesian approach employing Markov Chain Monte Carlo (MCMC), the value of the top-quark mass obtained is $m_t = 174.4^{+1.7}_{-2.7}$ GeV. From the comparison of the theoretical predictions for the absolute differential cross-section as a function of the invariant mass ($m_{t\bar{t}}$) with measured data in the lepton + jets channel at parton level, a second extraction of the top-quark mass has led to a value $m_t = 171.9^{+3.0}_{-2.9}$ GeV, obtained analysing the χ^2 between predicted and measured values.

Sommario

Lo studio della fisica del quark top rappresenta un campo in continuo sviluppo da parte della comunità teorica ed è di grande interesse all'interno del programma di fisica sperimentale ad ATLAS. In questa tesi, la massa del quark top è estratta mediante il confronto di calcoli di QCD della sezione d'urto totale e differenziale della produzione top-antitop in collisioni protone-protone ad energia del centro di massa di $\sqrt{s} = 13$ TeV, prodotti con il programma MATRIX al next-to-next-to-leading order, con dati sperimentali da collisioni pp a $\sqrt{s} = 13$ TeV raccolti nel 2015 e nel 2016 dal detector ATLAS al Large Hadron Collider (LHC) del CERN, corrispondenti a una luminosità integrata di 36.1 fb^{-1}. Utilizzando la sezione d'urto totale top-antitop ($t\bar{t}$) misurata in eventi dileptonici $e\mu$ e conducendo un'analisi basata su un approccio Bayesiano che utilizza Markov Chain Monte Carlo (MCMC), il valore ottenuto per la massa del quark top è $m_t = 174.4^{+1.7}_{-2.7}$ GeV. Dal confronto delle predizioni teoriche per la sezione d'urto differenziale assoluta in funzione della massa invariante ($m_{t\bar{t}}$) con dati misurati nel canale leptoni + jet a livello partonico, una seconda estrazione della massa del quark top ha portato al valore $m_t = 171.9^{+3.0}_{-2.9}$ GeV, ottenuto analizzando il χ^2 tra i valori della predizione e quelli misurati.

Contents

Introduction

The top-quark was discovered at Fermilab Tevatron in 1995, and it is the heaviest known fundamental particle to date. Thanks to its peculiar properties it represents one of the most interesting research fields in particle physics, as its study is not only fundamental for a more profound understanding of the Standard Model, the currently most complete theory describing particles and their interactions, but also in the exploration of physics Beyond the Standard Model (BSM), due to its large coupling with the Higgs boson. Because of its large mass, the production of the top-quark requires particle collisions at very high energies and the Large Hadron Collider (LHC) is the only existing facility able to produce a substantial number of top-quark events, therefore allowing for the measurement of the characteristics of the top-quark with high precision.
As a colour-charged particle, the top-quark is subjected to colour confinement, as are all other quarks, which leads to the impossibility of directly measuring its mass. Therefore, different mass parameters can be employed, depending on which one represents the most advantageous candidate for the characteristic scale of the process considered. In order to extract a well-defined quark mass parameter from experimental data it is necessary to compare predictions, expressed in the theoretical framework of interest, and observations that depend on the value of the quark mass. The production cross section is one of the most popular observables used in these comparisons.
In this thesis two extractions of the top-quark mass are presented. They are obtained from the comparison of theoretical predictions with data from proton-proton collisions at a centre-of-mass energy of $\sqrt{s}$=13 TeV collected by the ATLAS experiment in 2015 and 2016, corresponding to an integrated luminosity of 36 fb^{-1}. The theoretical calculations of the processes at NNLO are performed using the MATRIX program implemented on two multi-core machines, theophys02 and the HPC cluster 'MATRIX' of the Open Physics Hub of the Department of Physics and Astronomy of the University of Bologna. The first extraction is based on the $t\bar{t}$ production total cross-section in the dilepton channel, while the second is centred on measurements of the $t\bar{t}$ production differential cross-section in the lepton+jets channel.
This thesis is arranged as follows. Chapter 1 offers an overview of the Standard Model and of top-quark physics, while a rundown of the ATLAS experiment is given in Chapter 2. In Chapter 3 the program MATRIX and the theoretical predictions generated with it are introduced and described. Chapter 4 contains the comparison between the experimental

data collected at ATLAS and the predicted values for the production cross-section, as well as the two values extracted for the top-quark mass. Appendix A presents a broader description of the statistical methods employed in the top-quark mass extraction from the total cross-section measurement in the dilepton channel.

Chapter 1

Introduction to the Standard Model

The Standard Model (SM) of particle physics currently is the most complete theoretical framework that explains the basic building blocks of matter and the fundamental interactions between them. The SM successfully describes three of the four fundamental interactions of nature (the electromagnetic, weak and strong interactions, with gravity being the exception) through gauge theories, based on the symmetry group

$$U(1)_Y \otimes SU(2)_L \otimes SU(3)_c$$

resulting from the direct product of the three gauge simmetries required to describe the electro-weak and the strong interactions. The subscripts in the previous expression are used to highlight the gauge charges associated to the interactions considered: Y, the weak hypercharge that relates the electric charge to the third component of the weak isospin of a particle; L, a reminder that only matter particles with negative chirality (left-handed) are involved in phenomena mediated by the weak interaction; and c, the colour charge.
The SM is considered to be able to properly describe natural phenomena up to the Planck energy scale ($\approx 10^{19}$ GeV), as this is the scale at which the strength of gravity becomes comparable to that of the strong force. However, the inability of the Standard Model to incorporate gravity within its formulation poses one of the biggest limits of the model itself. Other such limits of the SM include the phenomenon of neutrino oscillation and the incapacity of the model to explain cosmological evidence of dark energy and dark matter, as well as the prevalence of baryonic matter over the antibaryonic one. On a theoretical point of view there is also the problem of the absence of CP violation observed in some phenomena involving the strong interaction and the hierarchy problem, concerning the mass of the Higgs boson. Nevertheless, since the predictions of the SM within the energy scales currently available are consistently in extremely good agreement with the experimental data, the shortcomings of the Model seem to point towards the existence of physics Beyond the Standard Model (BSM physics) rather than to a fallaciousness of the SM itself.

1.1 Particles and their interactions

The fundamental particles on which the SM is built upon can be divided in two categories, matter particles and force carriers. The elementary matter particles are fermions of spin $\frac{1}{2}$, as they are described by an asymmetric wave function that follows Fermi-Dirac statistics and obeys Pauli exclusion principle. As Dirac's equation [1] allows for both positive and negative energy solutions, the former are interpreted as particles and the latter as antiparticles, that share the same mass and spin as the corresponding fermions but have opposite charges. Elementary fermions are further divided into quarks and leptons, based on whether they do or do not bear the colour charge and therefore do or do not interact through the strong interaction, respectively. The six flavours of quarks (up, down, charm, strange, top, bottom) and the six flavours of leptons (three neutrinos, electron, muon, tau) are organised in three families of two fermions:

$$Leptons : \begin{pmatrix} \nu_e \\ e \end{pmatrix}, \begin{pmatrix} \nu_\mu \\ \mu \end{pmatrix}, \begin{pmatrix} \nu_\tau \\ \tau \end{pmatrix} \tag{1.1}$$

$$Quarks : \begin{pmatrix} u \\ d \end{pmatrix}, \begin{pmatrix} c \\ s \end{pmatrix}, \begin{pmatrix} t \\ b \end{pmatrix} \tag{1.2}$$

where leptons hold integer electric charge, equal to 0 for neutrinos (ν_e, ν_μ, ν_τ) and -1e[1] for electron-like leptons (e, μ, τ), while quarks have fractional electric charge, of $2/3e$ for up-like quarks (u, c, t) and -$1/3e$ for down-like quarks (d, s, b). Leptons are characterised by an additive quantum number, the lepton number, that is null for all other particles and assumes the value of 1 for leptons and of -1 for anti-leptons. For each family of leptons a different lepton number is defined (the electron-lepton number L_e, the muon-lepton number L_μ, the tau-lepton number L_τ) on the basis of properties of the weak interaction. These quantities are conserved separately and collectively (as the total lepton number) by almost all interactions of nature, with the exception of the phenomenon known as neutrino oscillation.
Quarks (and their bound states) are the only matter particles that bear the colour charge, that assumes three possible values in particles and three in antiparticles. Through this charge, quarks form singlet bound states known as hadrons, often referred to as colourless bound states. As singlet states are the only ones that have ever been observed in nature, quark can only be found within these bounds, a property called confinement. Hadrons can be further categorised into two groups:

- baryons (antibaryons), triplets of quarks (antiquarks) of semi-integer spin values and thus following the collective behaviour of fermions;

[1] $e = 1.6022 \cdot 10^{-19}$C

- mesons, pairs of quarks-antiquarks of integer spin value. As they are described by a symmetrical wave-function that obeys Bose-Einstein statistics, they follow the collective behaviour of bosons.

Although the number of quarks in the SM would allow for a great variety of hadrons, ordinary matter is only composed of two baryons that bind together to form the atoms' nuclei: positively charged protons, the sole truly stable hadrons in nature; and the neutrally charged neutrons, naturally instable but that gain stability within the bounds of the nuclei. The absence of matter more varied or exotic in nature is ascribable to the decay of heavier hadrons in lighter and lighter particles, until only protons and neutrons are left, as they are composed of only the lightest of quarks, up and down.
While particles are the fundamental constituents of matter, interactions are the ones that dictate how particles are brought together and how matter is formed. As a renormalisable field theory, the SM describes all particles as excited states, also known as quanta, of their underlying quantum fields, that are the true fundamental entities, contrary to what was originally believed in classical physics. Quantum Field Theory (QFT) incorporates special relativity, quantum mechanics and classical field theory, and requires that forces are to be mediated by particles with integer spin (vector bosons), as to allow for action at a distance, while preserving the relativity principles. Although as of today a theory of gravitation capable of incorporating quantum mechanics is not available, at the current accessible energy levels at particle scale its contribution can be considered negligible. In fact, experimental data shows that the interactions at play among the 12 material fields (and 12 antimaterial fields) are dominated by the three interactions described in the SM: electromagnetic interaction (Quantum Electro-Dynamics, or QED), weak interaction (Quantum Flavour Dynamics, or QFD) and strong interaction (Quantum ChromoDynamics, or QCD). The mediators of these interactions are bosons with spin equal to one; their names and some of their basic properties are displayed in Table 1.1.

Interaction	Relative strength	Range [cm]	Mediator	Symbol	Mass $[\frac{\text{GeV}}{c^2}]$
Strong	1	10^{-13}	Gluons	g	0
Electromagnetic	10^{-2}	∞	Photon	γ	0
Weak	10^{-5}	$< 10^{-15}$	W and Z	$W^{\pm}, Z$	≈ 100
Gravity	10^{-39}	∞	Graviton	G	0

Table 1.1: Representation of the four fundamental forces and their mediators. The mass is reported in GeV/c^2, while the range is expressed in centimeters [2]. The strength comparison of the four basic forces is meaningful only in relative terms. The graviton, the supposed mediator of gravity, is a spin 2 boson introduced in QFT, but yet to be included in the SM.

The set of fundamental particles of the Standard Model, see Figure 1.1, is completed

by a scalar boson with zero spin and with neither electric nor colour charge, the Higgs boson, H. The Higgs boson is the quanta produced by the excitement of the Higgs field, whose interaction with the other elementary particles through the Brout-Englert-Higgs (BEH) mechanism is responsible for furnishing the particles with their mass.

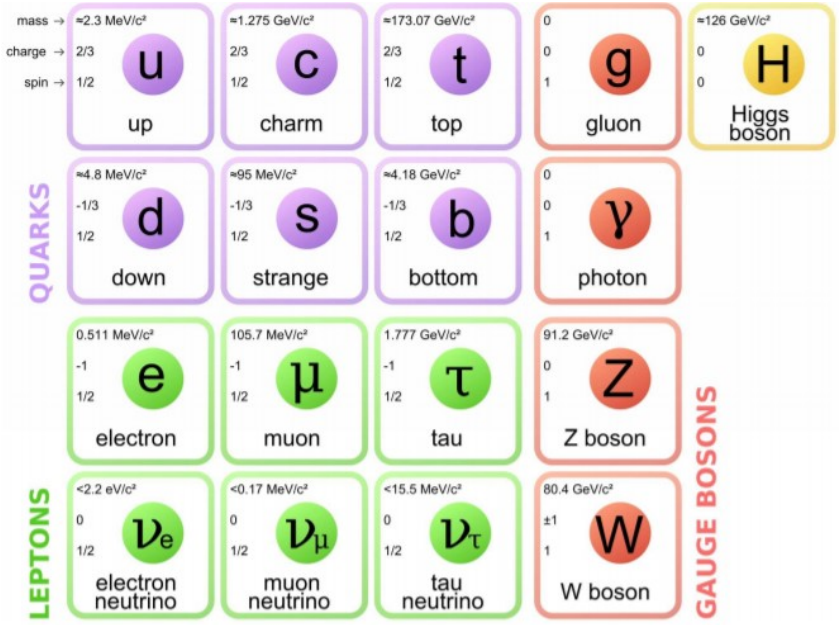

Figure 1.1: The fundamental particles of the Standard Model and some of their properties.

Quantum Electrodynamics (QED)

The electromagnetic interaction has been studied to great depth both in classical and quantum theory. Quantum Electrodynamics (QED), the quantum field theory that describes electrodynamics, is an abelian gauge theory with the symmetry $U(1)$ and it was the first instance of full agreement between quantum mechanics and special relativity. The photon (γ) is the quantum of the electromagnetic field and it is a mass-less, charge-less boson of spin 1. Since its mediator does not have a mass, the electromagnetic interaction has an infinite range of action, while the photon's lack of an electric charge forbids it from self-interacting. The strength of the electromagnetic interaction is inversely proportional to the square of the distance between the particles and directly proportional to the coupling constant [3]:

$$\alpha = \frac{1}{4\pi\epsilon_0}\frac{e^2}{\hbar c} \approx \frac{1}{137}. \tag{1.3}$$

As in QFT the interaction between two particles is described in terms of probability of transition between two states, Feynman diagrams are often used to properly assess

the phenomena under scrutiny. Since the coupling constant $\sqrt{\alpha}$ of the electromagnetic interaction is smaller than one, QED can be described as a perturbative theory of the electromagnetic quantum vacuum.

Quantum Flavour Dynamics (QFD) and Electro-Weak Theory (EWT)

Despite the great variety of particles discovered in accelerators and colliders, ordinary matter is only composed of electrons, protons and neutrons. The absence of mesonic or baryonic matter of more exotic nature is ascribable to the action of the weak interaction. This force, due to its lower strength when compared to that of the electromagnetic or strong interaction, is usually stifled by the others and the particles for whose decay it is responsible have a characteristically longer lifetime. The weak interaction breaks quite a few symmetries that both the electromagnetic and the strong interaction conserve, first of all the conservation of flavour. Quarks decay into one another with different probabilities: the flavour changing preferably occurs within the same family, but decays across generations are nonetheless possible, with a sensitively lower probability. The mixing between families is described by the CKM matrix, introduced by Cabibbo, Kobayashi and Maskawa [4, 5],

$$\begin{bmatrix} d' \\ s' \\ b' \end{bmatrix} = \begin{bmatrix} V_{ud} & V_{us} & V_{ub} \\ V_{cd} & V_{cs} & V_{cb} \\ V_{td} & V_{ts} & V_{tb} \end{bmatrix} \begin{bmatrix} d \\ s \\ b \end{bmatrix} \tag{1.4}$$

which is also highly relevant when considering the CP (charge-parity symmetry) violation. In fact, the weak interaction is also the only interaction that violates parity symmetry (p-symmetry) and CP symmetry simultaneously.

Differently from QED, the weak interaction is mediated by three charged massive bosons: $W^{\pm}$ for charged current interaction (CC), and Z for neutral current interaction (NC). The mass of these mediators, far larger than that of most quarks (with the sole exception of the top quark), is consistent with the short range of the weak force and has been introduced in the theory thanks to the unification of electromagnetic and weak theory and the spontaneous symmetry breaking proposed by Anderson, Higgs [6], Englert and Brout [7] in 1964. Above the unification energy, of the order of 246 GeV, QED and QFD would merge into a single force, the electroweak interaction [8, 9, 10].

Electro-Weak Theory (EWT) is a Yang–Mills theory based on an $SU(2) \otimes U(1)$ gauge group, whose generators, the electro-weak isospin T and the hypercharge Y, give rise to the gauge bosons that mediate the electroweak interactions: the three W bosons of weak isospin ($W1$, $W2$, and $W3$), and the B boson of weak hypercharge. Originally massless, these bosons would combine into actual physical fields through spontaneous symmetry breaking and the associated Higgs mechanism.

By adding to the SM Lagrangian a scalar field (Higgs field) that permeates the vacuum and interacts with both the matter fermion fields and the weak field, the W and Z bosons

would acquire mass by the interaction with the Higgs field through the spontaneous symmetry breaking of the Lagrangian (BEH mechanism), leaving the photon mass-less. The interaction between the Higgs field and the fermion fields is also the origin of the mass of fermions. The theory includes the quantum of the scalar Higgs field: a massive, chargeless boson, the Higgs boson, whose existence was proved and announced by ATLAS [11] and CMS [12] experiments on 4 th of July 2012 at CERN, effectively confirming the validity of this theory.

Quantum Chromodynamics (QCD)

Quantum Chromodynamics (QCD)[13, 14] is the SU(3) gauge field theory that describes the strong interaction between coloured quarks and gluons. The colour charge was initially introduced to explain the existence of observed particles such as Ω^-, that is a bound state of spin 3/2 composed of three s-quarks, that seemed to break the Pauli principle. As a state formed by an uneven number of fermions it should be anti-symmetric, but the wave function of this particle is completely symmetrical, with 3 quarks with aligned spins and the same quantum numbers. Hence, an additional internal degree of freedom must be considered to allow for the existence of anti-symmetric states formed by 3 quarks with the same spin and flavour. Such a role was attributed to the colour charge, a vector in a three-dimensional complex space, whose different states have three possible values. The interaction between quarks is invariant under colour interchange, therefore the colour charge can be interpreted as the gauge charge of the strong interaction.
The mediators of the strong interaction are an octet of massless, spin 1 bosons, the gluons, that are colour-charged, each carrying a colour and an anti-colour.
Since QCD is a non-Abelian gauge theory and the gluonic fields carry colour charges, the gluons are self-interacting and 3 or 4 gluon vertices are allowed (see Figure 1.2).

Figure 1.2: Allowed self-coupling gluon vertices.

The most distinctive features of the strong interaction originate from the self-interaction of gluons and are connected to the dependence of the strong coupling constant on the transferred momentum: for momentum transfers in the range 100 GeV – 1 TeV $\alpha_S \approx 0.1$, while the QCD is strongly interacting for scales around and below 1 GeV.
As the coupling grows with the distance, at large separation between quarks (or small transferred momentum) the strength of the interaction increases and it becomes im-

possible to separate quarks. This leads to the impossibility of observing free quarks, a property called colour confinement, often observed in high-energy scattering processes. When trying to extract quarks or gluons from within a hadron, one incurs into hadronization, a process where gluon radiation and the branching of the scattered particles cause the production of a number of colour singlet hadrons.
Increasing the energy scale of the interaction, and correspondingly decreasing the length scale of the process, the strong coupling tends to zero and quarks behave asymptotically as free particles, a property aptly named asymptotic freedom.

1.2 The top-quark

Among the fundamental particles in the SM, the top quark distinguishes itself as the heaviest elementary particle, with a mass at least two order of magnitude heavier than that of the other quarks, as well as for the fact that it is the only quark that decays before hadronisation, thus representing a chance of examining a bare quark through the study of its decay products. The top quark was first discovered at Fermilab Tevatron in 1995 [15, 16] and today it is extensively studied at the Large Hadron Collider, where a higher production rate can be achieved. An accurate study of top-quark production processes and properties, might lead to a deeper knowledge of the Standard Model as well as possibly being a probe towards physics Beyond the Standard Model (BSM physics), especially when considering the strong coupling between the top quark and the Higgs boson.

1.2.1 Discovery

The existence of the top quark had been predicted a long time before its actual discovery, ever since the introduction of a third family of quarks and leptons by Kobayashi and Maskawa in 1973 [5], out of necessity to describe the CP violation in the weak interaction. The discovery of the lepton τ two years later, in 1975 [17], consolidated the theory of the presence of a third family of quarks as well. In 1977 the existence of the first member of this third generation was proved when the collisions at Fermilab produced the bottonium (Υ) [18, 19, 20], thus introducing the fifth quark, the bottom. The discovery of the last quark seemed to be very close, however its actual discovery came about two decades later, after many attempts at detection. The difficulties in the discovery of the top quark came from the fact that this particle possessed a mass far larger than expected, and the experimental facilities of the time were not energetic enough to allow for the production of top quarks from collisions, only being able of setting lower bounds to the value of the top quark mass. Thanks to the progress in particle accelerator techniques, the discovery of the top quark came in 1995, by the experiments CDF and D$\emptyset$ at Fermilab's Tevatron [15, 16].

1.2.2 Properties and role of the top-quark in the SM

The top quark is a massive fermion of spin $\frac{1}{2}$, of the up-type quality (charge $+\frac{2}{3}e$) in the third family of elementary particles.
The top quark is the heaviest elementary particle of the SM, with a mass close to that of a Rhenium atom (Z=75). The large mass of this particle is of high relevance in the study of top-quark properties since it is at the origin of the whole phenomenology of this quark. As it its mass is above the Wb threshold, the decay width of the top quark is dominated by the two-body decay channel (see Figure 1.3):

$$t \to Wb, \tag{1.5}$$

while other Ws or Wd decays are supressed by the CKM matrix. Therefore, the lifetime of the top quark $\tau_t \approx 10^{-24}$ s is shorter than the average time for hadron formation by an order of magnitude, leading to the absence of top-flavoured hadrons or $t\bar{t}$-quarkonium bound states. As a consequence, the top quark can be reconstructed from its decay products, thus giving a unique chance to study the properties of a bare quark.
Another interesting field of study is the the coupling of the top quark to the Higgs boson, the so-called Yukawa coupling which is defined in the Standard Model as

$$\lambda_t = \sqrt{2}\frac{m_t}{v} \tag{1.6}$$

where v is the Higgs field expectation value in vacuum and m_t is the top-quark mass. As the top quark is the fermion with the highest value of this coupling, the study of top-quark physics could enable the access to numerous speculations related to new physics and BSM physics.

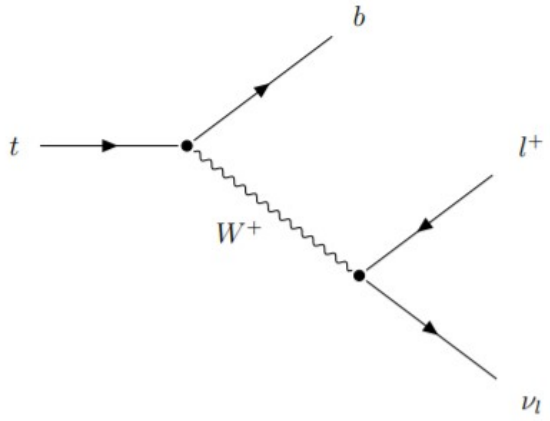

Figure 1.3: Example of decay channel of t quark into W^+ and b with subsequent leptonic decay.

Problems related to the definition of the top-quark mass

The mass of the top quark has been experimentally extracted through the study of its decay products, a W boson and a b-quark, and it has been compared to theory predictions. Quark masses enter the QCD Lagrangian as bare parameters and are subject to quantum loop corrections at higher orders. Therefore, their values depend on a certain choice of the renormalisation scheme. The value determined through experimental data is conventionally identified with the pole mass, especially in the context of the global electro-weak fit, which is obtained via the on-shell renormalisation scheme and defined as the real part of the pole in the top-quark propagator:

$$\sqrt{p^2} = m^{pole} - \Gamma\frac{i}{2} \tag{1.7}$$

where p is the 4-momentum and $\Gamma \approx 1.5$ GeV is the top-quark decay width [21]. The propagator yields a peak in the Wb invariant-mass distribution (for real values of p that are accessible experimentally) when $\sqrt{p^2} \approx m^{pole}$.

This definition of the pole mass is gauge invariant at each order of perturbation theory, however, the employment of the pole mass has been often argued upon due to the presence of infrared renormalon ambiguity, as a result of nonperturbative QCD. This notion is physically in good agreement with the theory that quarks are confined within hadrons and hence do not generate poles in a complete QCD calculation, making an unambiguous definition of a pole mass impossible.

An alternative way to define the top quark mass is based on the $\overline{MS}$ scheme, where the mass is running (scale dependent), analogous to a coupling constant that needs to be specified at a given scale μ. The pole mass m_t^{pole} and the $\overline{MS}$-mass $m_t^{\overline{MS}}$ are related via

$$m_t^{pole} = m_t^{\overline{MS}}(R,\mu) + \delta m_t(R,\mu) \tag{1.8}$$

where R and μ are scale parameters and the corrections in δm_t are known to four loops in QCD [22].

Theory wise, as most top-quark mass extractions use Monte Carlo shower codes, one customarily defines the quantity determined as "Monte Carlo mass". Then again, one refers to pole or $\overline{MS}$-mass extraction whenever an estimation is compared to a fixed-order, possibly ressumed, QCD computation using a given field-theory mass definition.

Another topic of discussion has been the distinction between Monte Carlo and well-posed mass definitions like the pole mass. However, even pole mass determinations are not completely independent from the Monte Carlo method, as the assessment of the experimental acceptance mildly depends on which shower code and mass parameter are employed.

Other well-posed mass definitions often used to interpret the measurements of the top-quark mass at LHC, whose explicit expressions and relations to the pole mass can be found at [23], are:

- The 1S mass, defined as half the mass of a fictitious $\Upsilon(1S)$ resonance, made up of a bound $t\bar{t}$ state.

- The potential-subtracted (PS) mass, which is constructed in terms of the $t\bar{t}$ Coulomb potential. To suppress renormalons, contributions below a factorization scale μ_F are subtracted.
- The renormalon-subtracted (RS) mass, another threshold mass that removes from the pole mass the pure renormalon contribution.
- The kinetic mass, that was defined for the purpose of improving the convergence of the perturbative expansion of the semi-leptonic B-meson decay width.

Since the 1S, PS and RS masses are threshold masses they do not exhibit the renormalon ambiguity that affects the pole mass.
The issue of identifying the real meaning of the top-quark mass has been regarded as an academic speculation for many years, because before the LHC operations the experimental uncertainties were much larger than the theoretical ambiguities. Nowadays, thanks to the new data and the significant uncertainty reduction, it is a hot topic that animates the scientific debate.

EW precise measurements involving the top mass

At the Tevatron and the LHC, top quarks and antiquarks are mainly produced in pairs via gluon fusion or through the annihilation of accelerated quark-antiquark particles. The two accelerators have a few differences when it comes to production processes, mainly related to the different energy scales at which the processes unfold, as the LHC allows for a higher centre-of-mass-energy, and the type of beams employed in the collisions, proton-antiproton at Tevatron and proton-proton at the LHC. At Tevatron these processes are dominated by $q\bar{q}$ annihilation, while at the LHC the dominant phenomenon is gluon-gluon fusion. The Feynmann diagrams of these processes are shown in Figure 1.4.

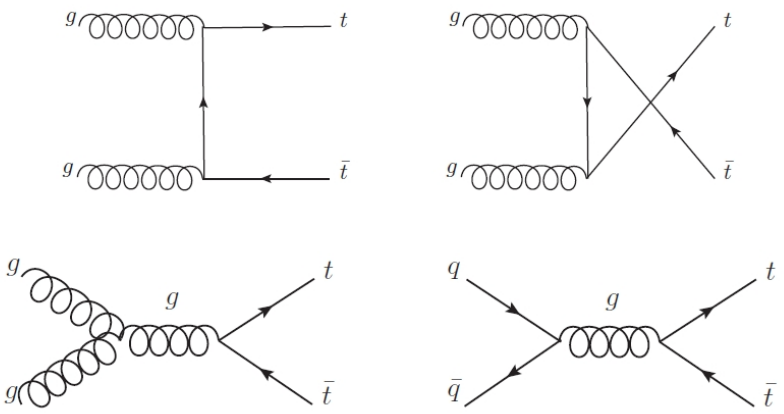

Figure 1.4: Production diagrams of $t\bar{t}$ pairs at leading order.

The top quark decays almost exclusively, with a branching ratio of 99.8%, to a W boson and a bottom quark, due to the near unity (0.999146 [24]) of the corresponding CKM matrix entry. Therefore, the decay of the W bosons is the characterising element of the experimental signature of $t\bar{t}$ production: the all hadronic decay channel (with a branching fraction of 46%) has four light quarks and two b quarks in the final state; the semi-lepton decay mode (44%) involves one hadronic and one leptonic W boson decay and thus has two light quarks, two b quarks, one charged lepton and one neutrino in its final state; and finally, the full leptonic decay channel (10%) involves two b quarks, two oppositely charged leptons and two neutrinos [22].
In addition to experimental uncertainties, one needs to consider the uncertainties related to the modelling of top-quark pair production and decay as well. This modelling depends on the choice of the proton PDFs, the order in α_s of the perturbative QCD computation, additional initial and final state radiation and the associated parton shower modelling, as well as the choice of the underlying event and hadronisation model.
Generally, the most precise determinations of m_t^{MC} are achieved in the semi-leptonic decay channel, while the di-lepton channel usually has the best signal-to-background ratio, with the negative side of having two decay neutrinos in the final state, which forbids a complete kinematic event reconstruction. The full hadronic decay channel has the worst signal to background ratio, but it has the advantage of being able to fully reconstruct the event kinematics as no neutrinos are involved. Once top-quark pair events are selected and background contributions estimated, several approaches to measure m_t can be pursued. All direct m_t measurements are based on information about the reconstructed kinematics of the measured decay products and their combinations. Three methods, all of which determine the top-quark mass parameter in the underlying Monte Carlo event generator but not directly the pole or the MS mass, have recently been used for the precision measurement of m_t: the template method [26]; the matrix element method [27]; and the ideogram method [28]. A recent summary plot for the direct top-quark mass measurements realised at ATLAS and CMS is shown in Figure 1.5.
An alternative method to determine m_t^{pole} is based on the mass dependence of the $t\bar{t}$ production cross-section, $\sigma_{t\bar{t}}$, which can be written as a convolution of the parton density functions (PDFs) and partonic cross-section $\hat{\sigma}$ [29]:

$$\sigma_{pp\to t\bar{t}}(s, m_t) = \sum_{i,j=q,\bar{q},g} \int dx_i dx_j f_i(x_i, \mu_f^2) f_j(x_j, \mu_f^2) \cdot \hat{\sigma}_{ij\to t\bar{t}}(\hat{s}, m_t, \mu_f, \mu_r, \alpha_s) \qquad (1.9)$$

where f are the PDFs and $\hat{s}$ is the centre-of-mass energy. The sum runs over all partons (quark, anti-quark and gluons), and μ_f and μ_r are the factorization and renormalization scales, two cut-offs whose presence is required when dealing with the infrared and ultra-violet divergences that arise in finite order calculations. As higher and higher orders are included in the perturbative calculation, the dependence of the cross-section on these two scale becomes weaker.

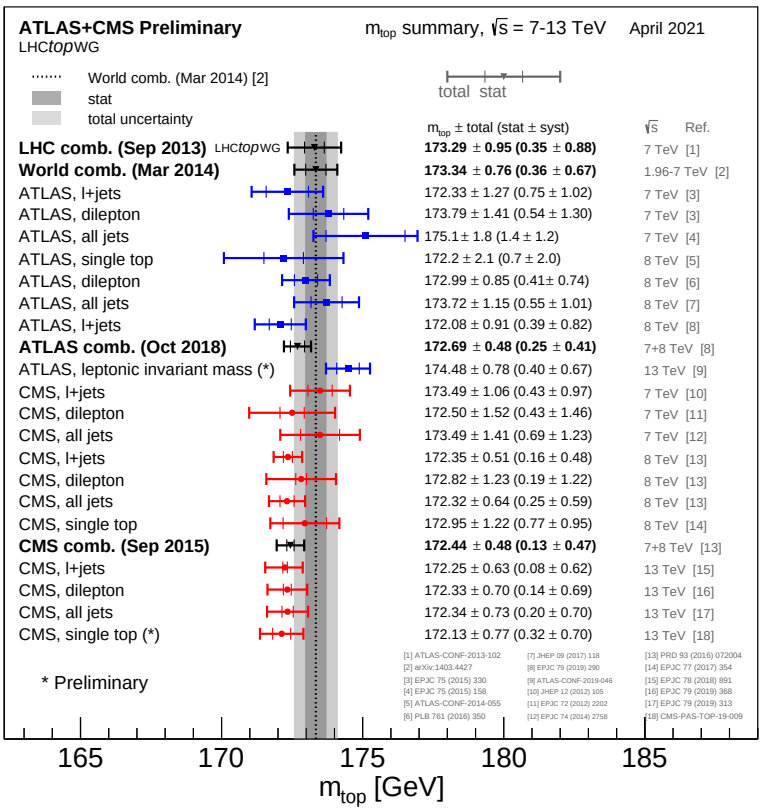

Figure 1.5: Summary of the ATLAS and CMS direct m_t measurements. The results are compared with the LHC and Tevatron+LHC m_t combinations [25]

The cross-section $\sigma_{t\bar{t}}$ can be expressed directly in terms of the pole mass or some other convenient mass definition, therefore, the value of m_t^{pole} can be determined from its precision measurement. For further information and an easier comparison with theoretical models, differential cross-section measurements are often employed, usually at particle level, in which one refers to quantities directly measurable in the detector, or at parton level, which refers to the true kinematic quantities of the produced top quarks, that need to be extrapolated to the full phase space. A recent summary plot for the top-quark mass measurements extracted from the cross-section, realised at ATLAS and CMS is shown in Figure 1.6.
A combination of measurements of the mass of the top quark, m_t, performed by the CDF and $D\emptyset$ experiments at the Tevatron collider and the ATLAS and CMS experiments at the Large Hadron Collider (LHC) has led to the value:

$$m_{top} = 173.34 \pm 0.27(\text{stat.}) \pm 0.71(\text{syst.})\text{GeV} \tag{1.10}$$

with a total uncertainty of 0.76 GeV [30].

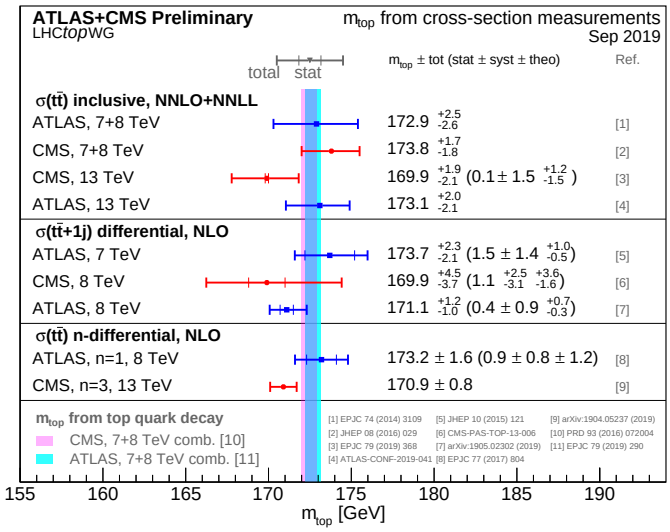

Figure 1.6: Summary of the ATLAS and CMS measurements of the top quark mass from $t\bar{t}$ production observables. The results are compared with the ATLAS and CMS combination of measurements from top-quark decay. [25]

Top-quark mass and vacuum stability

The fact that all the parameters of the SM have been now experimentally determined tightly constrains the model and possibly BSM physics. If it exists, New Physics (NP) should have a marginal effect on the SM electro-weak fit, without spoiling its very good agreement with the experimental results. In this situation it is natural to wonder where the scale of NP is, or if it can be as large as the Planck scale, M_{Pl}, implying that the validity of the SM can be extended up to M_{Pl}. A course to answer this question is to study the stability of the SM vacuum, or to question whether the electro-weak (EW) minimum we live in is the true minimum of the SM effective potential, specifically the radiatively corrected scalar potential [31].

To study this scenario, one needs to possess knowledge of the Higgs effective potential $V_{eff}(\phi)$ up to very high values of ϕ. Due to top-quark loop corrections, $V_{eff}(\phi)$ bends down for values of ϕ much larger than v, the location of the electro-weak minimum, and develops a new minimum at $\phi_{min} \gg v$. Depending on Standard Model parameters, particularly the top-quark and Higgs masses (m_t and m_H), the second minimum could be higher, in which case the EW vacuum is stable, or lower than the EW one, which leads either to metastability or to instability. The discerning factor, in the second case, is whether the lifetime τ of the false EW vacuum is larger or shorter than the age of the universe T_U. If τ is larger than T_U, even though the EW vacuum is not the absolute minimum of $V_{eff}(\phi)$, our universe could be residing on a metastable vacuum, a phenomenon called metastability scenario.

According to the resulting stability phase diagram in Figure 1.7, for the current

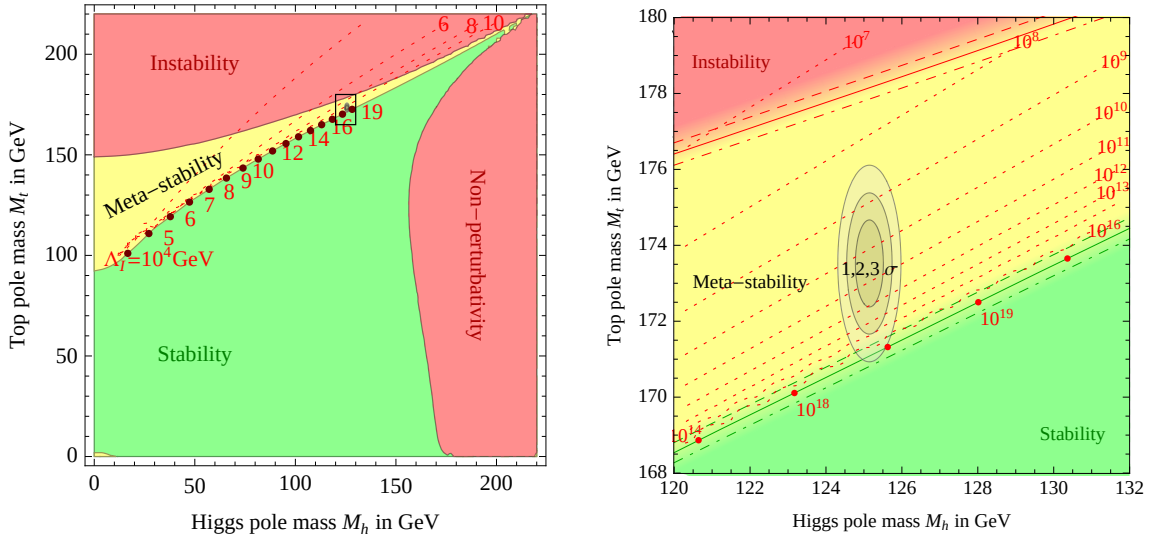

(a) (b)

Figure 1.7: **a:** SM phase diagram in terms of Higgs and top-quark pole masses. The plane is divided into regions of absolute stability, meta-stability and instability of the SM vacuum. **b:** Zoom in the region of the preferred experimental range of m_H and m_t^{pole} (the grey areas denote the allowed region at 1, 2, and 3σ). Plots taken from [32].

experimental values of the top-quark and Higgs masses, our universe lives in a metastable state (with very long lifetime), near the edge of stability. On the left, the different regions of stability of the EW vacuum are shown for a broad range of m_H and m_t, while on the right a zoom into the region corresponding to the measured values can be found. The measured values of m_H and m_t appear to be rather special, as they place the SM vacuum at the border between stability and metastability.

Due to the great sensitivity of the results on the stability analysis to the value of the top mass, it is commonly believed that a more precise measurement of m_t would lead to a definite answer to the question of whether the universe is located in the stability, in the metastability, or at the edge of stability (criticality) regions.

However, while an accurate determination of top-quark pole mass is of great importance and relevance, it has been shown that as long as the specific form of new physics is unknown, even in the possibility of NP interactions occurring only at the Planck scale, it is not possible to discriminate the stability condition of the EW vacuum [33].

Chapter 2

LHC and the ATLAS detector

The European Organisation for Nuclear Research (CERN) is a European research organization that operates the largest particle physics laboratory in the world, that shares its name. Since its establishment in 1954, the main research topics of CERN have moved from Nuclear Physics to High Energy Physics, but it also is one of the leading institutions in the development of new detector technologies and computing facilities. CERN hosts the largest proton accelerator of the world, the Large Hadron Collider (LHC), that houses four experiments, Alice [34], LHCb [35], CMS [36] and ATLAS [37].

2.1 The Large Hadron Collider

The Large Hadron Collider (LHC) is the latest accelerator built at CERN, as well as the largest and most powerful particle accelerator and collider ring ever built in the whole world. The LHC was installed in the existing 26.7 km tunnel that was constructed between 1984 and 1989 for the CERN LEP (Large Electron-Position) machine, CERN's previous biggest accelerator, located beneath the France–Switzerland border near Geneva. The LHC tunnel is divided into eight straight sections and eight arcs and lies between 45 m and 170 m below the surface. The LHC is designed to reach up to 14 TeV centre-of-mass collision energies ($\sqrt{s}$), with a peak instantaneous luminosity $\mathcal{L} = 10^{34}\text{cm}^{-2}\text{s}^{-1}$, and it aims for a high-precision study of the Standard Model and it searches for possible first evidence of new physics beyond it.
The LHC is designed as a proton-proton collider with separate magnet fields and vacuum chambers in the main arcs and with common sections only at the insertion regions where the experimental detectors are located [38]. The accelerating system consists of 16 radiofrequency cavities with a maximum electric field of 5.5 MV/m. A sophisticated magnet system, comprised of 1232 electromagnets that operate in superconducting state at a temperature of 1.9 K, drives the two proton beams around the accelerator in opposite directions, by creating a magnetic field of approximately 8 T. The focusing system

is made up of 392 quadrupoles of superconducting magnets that produce a 6.8 T field. The proton beams are accelerated to 450 GeV before entering the LHC using a sequence of accelerators: the linear accelerator (Linac2) and three synchrotrons, the PSB (Proton Synchrotron Booster), the PS (Proton Synchrotron), and the SPS (Super Proton Synchrotron). The accelerating chain of the LHC is shown in Figure 2.1.
The two pipes, where the beams circulate in opposite directions, intersect at four interaction points, where four detectors. These experiments are:

- ATLAS (A Toroidal LHC ApparatuS), a multipurpose experiment built to perform precise measurements in particle physics;
- CMS (Compact Muon Spectrometer), a multipurpose experiment like ATLAS, with which it shares the same goals, but pursues them with different and complementary technologies;
- LHCb, designed with the main goal of performing accurate measurements regarding bottom-quark physics in order to investigate the source of CP violation observed in nature;
- ALICE (A Large Ion Collider Experiment), dedicated to the study of quark-gluon plasma by reconstructing and analysing the collisions produced using ion-ion or proton-ion beams.

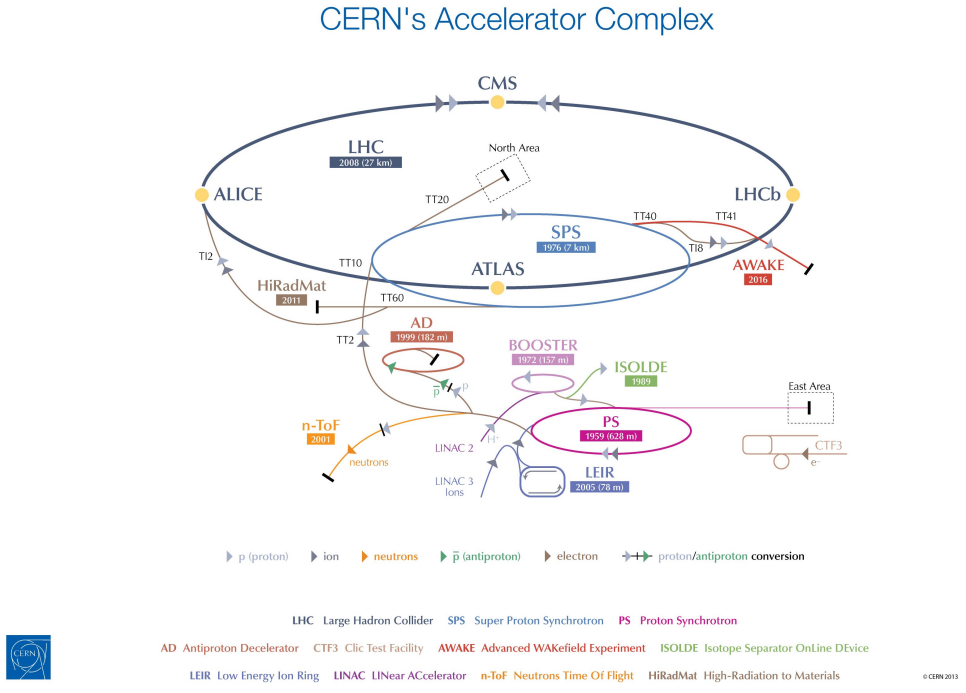

Figure 2.1: Illustration of the structure of the LHC facility at CERN, with its injection chain and the four main experiments performed on the ring.

The number of events per second for a particular process ($\frac{dN_{proc}}{dt}$) generated in the LHC collisions is proportional to the collider instantaneous luminosity $\mathcal{L}$:

$$\frac{dN_{proc}}{dt} = \mathcal{L}\sigma_{proc} \tag{2.1}$$

where σ_{proc} is the cross section for the process under study. In a machine such as the LHC, the luminosity can be expressed in terms of machine and beam parameters as [39]

$$\mathcal{L} = \frac{N_b^2 n_b f_{rev} \gamma_r}{4\pi\epsilon_n \beta^*} F \tag{2.2}$$

where N_b is the number of protons per bunch (of the order of $O(10^{11})$), n_b the number of bunches per beam (almost 2808 for each beam, with a nominal bunch spacing of 25 ns) and f_{rev}= 11.25 kHz the revolution frequency. γ_r is the relativistic gamma factor, ϵ_n=3.75μm the normalized transverse beam emittance, β^* the beta function at the collision point, and F the geometric luminosity reduction factor due to the crossing angle at the interaction point (IP):

$$F = \left(1 + \left(\frac{\theta_c \sigma_z}{2\sigma_{xy}}\right)^2\right)^{-\frac{1}{2}}. \tag{2.3}$$

Here, θ_c is the full crossing angle at the IP, σ_z and σ_{xy} are the RMS bunch length and the transverse RMS beam size at the IP, respectively.

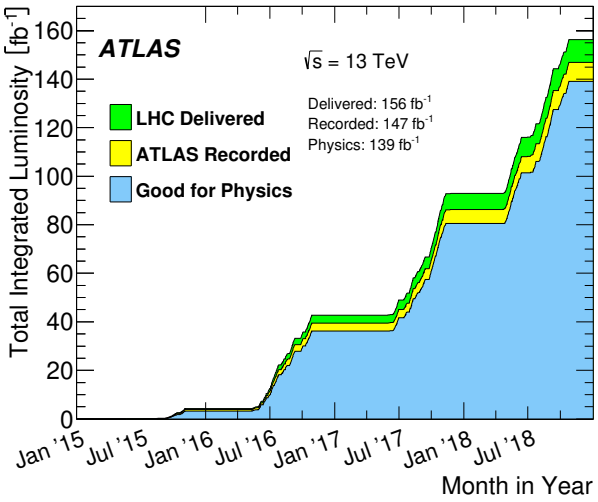

Figure 2.2: Cumulative integrated luminosity delivered to and recorded by ATLAS between 2015 and 2018 during stable beam pp collision data-taking at $\sqrt{s}$=13 TeV [40].

The integral of the instantaneous luminosity with respect to time, called the integrated luminosity (usually measured in fb^{-1}), is a measure of collision data collected;

$$L = \int_0^t \mathcal{L}\, dt = N_{proc}\sigma_{proc} \tag{2.4}$$

where N is the number of events produced for a process with cross section σ_{proc}.
The LHC delivered an integrated luminosity of 5.6 fb^{-1} of proton-proton collision data at the centre-of-mass energy of 7 TeV in 2010 and 2011. In 2012 the energy was increased to 8 TeV and the LHC luminosity was upgraded significantly and ATLAS recorded an amount around 14.3 fb^{-1} [41]. During the Run-2 period, from 2015 to 2018, at a $\sqrt{s} = 13$ TeV, it collected a total integrated luminosity of 139 fb^{-1}, as displayed in Figure 2.2.

2.2 The ATLAS detector

ATLAS is a general purpose detector [37], built for probing proton-proton collisions at very high energies, that aims to perform precise SM measurements. ATLAS is the largest experiment at LHC, with a cylindrically symmetric detector that is 42 meters long, with a radius of 11 meters and a weight of approximately 7000 tons, as illustrated in Figure 2.3.

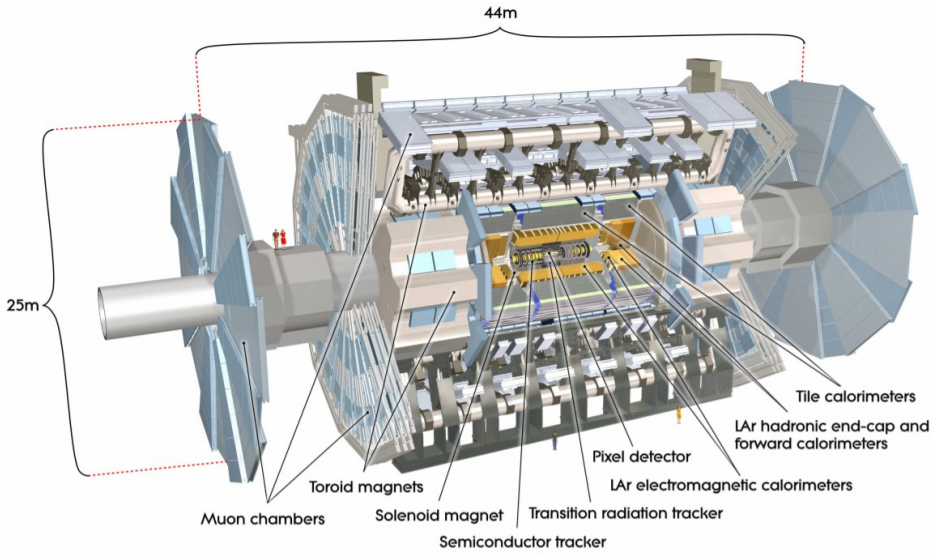

Figure 2.3: Cut-away view of the ATLAS detector.

The nominal interaction point (IP) is defined as the origin of the right-handed coordinate system placed at the centre of the detector, while the beam direction defines the z-axis. The positive x-axis points from the interaction point towards the centre of the LHC ring and, therefore, the positive y-axis is defined as pointing upwards. Due to

the cylindrical symmetry of the system, a set of polar coordinates (r, ϕ, θ) is employed, where the azimuthal angle ϕ is measured around the beam axis, and the polar angle θ is the angle from the beam axis. The pseudo-rapidity (η) is defined as $\eta = -\ln(\tan(\theta/2))$ and it is commonly used to describe the relative angle between a particle and the beam axis, with the forward direction referring to the region close to the beam axis, which corresponds to high values of $|\eta|$.
ATLAS is composed by a number of sub-detectors, that are involved in different stages of the reconstruction of the particles crossing the detector. The inner detector (ID) is composed of the core layers and is immersed in a magnetic field of 2T generated from a solenoid. It serves as tracking system and reaches a coverage $|\eta| < 2.5$. The calorimetry system forms the middle part of the ATLAS detector and extends the coverage up to $|\eta| = 4.9$. The calorimeters are responsible of measuring the energy of most of the particles while preventing them from entering the outermost layer, the muon spectrometer (MS). The task of the MS is the identification and reconstruction of muons, with a coverage of $|\eta| < 2.5$.

2.2.1 The Inner Detector

The inner detector is an important part of the tracking system of ATLAS, and its purpose is to identify and reconstruct tracks and vertices within the dense environment of the LHC, where several protons can collide at the same time. In order to distinguish the origin of the tracks and measure the bending of the particles caused by the magnetic field surrounding the ID, high-precision measurements must be made with fine detector granularity. The ID is composed of three sub-sections (see Figure 2.4): the silicon pixel detector, the micro-strip detector (SCT) and a straw-tube tracking detector (TRT). The detectors with higher granularity (pixels and SCT) are based on silicon technology and arranged on concentric cylinders around the beam axis. In the end-cap regions they are located on disks perpendicular to the beam axis.

2.2.2 The Magnet System

The trajectory of a charged particle moving in an external magnetic field, if projected on a plane orthogonal to the field direction, is deflected into a circular orbit whose radius is proportional to the particle's momentum transverse to the field direction, as for the Lorentz force law. Therefore, the transverse momenta of the charged particles crossing the ATLAS detector is determined by measuring the track bending caused by the detector's magnetic field.
The ATLAS magnet system is composed of four superconducting magnets, three toroids and a solenoid, that provide a magnetic field covering a volume of 12,000 m^3. The solenoid is aligned with the beam axis and provides a constant 2T axial magnetic field for the inner tracker and its layout was carefully optimised upon its construction to

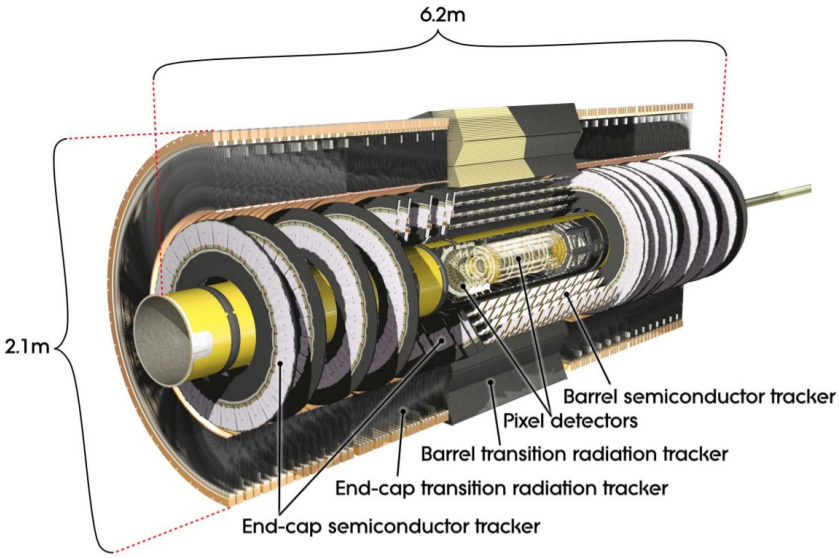

Figure 2.4: Cut-away view of the inner detector.

minimise the radiative thickness in front of the calorimeter system. The three air-core toroid magnets provide the magnetic field for the MS: two end-cap toroids (ECTs) that are inserted in the barrel toroid (BT) at each end and line up with the central solenoid. The barrel toroid coils are housed in eight individual cryostats, while each end-cap toroid consists of eight racetrack-like coils in an aluminium alloy housing. An illustration of the geometry of the magnetic system is provided in Figure 2.5.

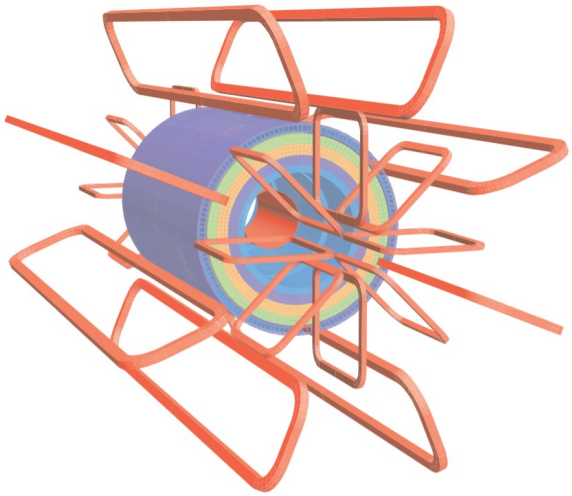

Figure 2.5: Geometrical representation of the magnet system and the tile calorimeter steel. The eight barrel toroid coils, with the end-cap coils interleaved, are visible.

The BT provides the bending power in the region $0 < |\eta| < 1.4$, while in the range $1.6 < |\eta| < 2.7$ charged tracks are bent by the ECTs. In the transition region, $1.4 < |\eta| < 1.6$, the magnets overlap, leading to a reduced bending power of the combined magnetic field. Nevertheless, the field is almost orthogonal to the muon flight direction, with an approximate value of 3T in the barrel and of 6T in the end-caps, which allows for measurements of the muons' momentum in the TeV range.

2.2.3 The Calorimetry System

The Calorimetry System is designed to trigger and precisely reconstruct all the neutral and charged particles that produce showers: electrons, photons and hadrons. Since they allow for the measurement of the visible energy in the event in the plane transverse to the beam pipe, the calorimeters are fundamental in the reconstruction of the neutrinos as missing transverse energy, as well. As the particles that end in showering are completely different in composition and in the type of interaction involved, their longitudinal and transverse evolution differs as well. Therefore, different technologies must be employed to reconstruct with high precision the diverse kinds of shower. Incident electromagnetic particles, i.e. electrons and photons, initiate a relatively short and concentrated electromagnetic shower and are fully absorbed by Electromagnetic Calorimeters (ECs). Incident hadrons, on the other hand, may start showering in the electromagnetic calorimeter but then be fully absorbed only in the surrounding Hadronic Calorimeter (HC).
The coverage of the calorimetry system reaches $|\eta| < 4.9$ and its structure is shown in Figure 2.6.

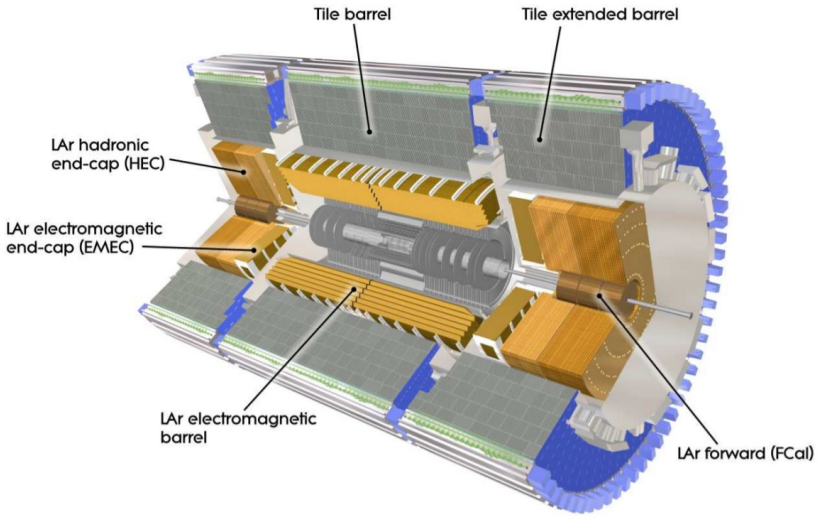

Figure 2.6: Cut-away view of the ATLAS calorimetry system

The calorimeters are located around the solenoid, and they occupy a large volume of the ATLAS detector, since they must completely contain the showers, therefore preventing particles different from the muons from accessing the Muon Spectrometer.
The thickness of the calorimeter depends on the material and the type of interaction with impacting particles and it is usually quantified in terms of the radiation length (X_0). X_0 is defined as the average distance that must be covered to reduce the energy of an electron by a factor $1/e$. When considering the hadronic showers, a similar quantity is introduced, the nuclear interaction length (λ), which is defined as the mean length required to reduce the numbers of relativistic charged particles in the shower by the factor $1/e$. The total thickness of the EC is more than 22 radiation lengths in the barrel and 24 in the end-caps, while the length of the HC is 9.7 interaction lengths (10 in the end-caps), sufficient to provide good resolution for high-energy jets as well.
Both the HC and EC are sampling calorimeters, which means that they are composed by alternating layers of absorbing and active material. The absorbing material produces the electromagnetic and hadronic showers by maximising the interaction with the particles, while the active layer has the task of measuring the energy of the original incident particle. The use of sampling calorimeters is advantageous in that they provide excellent shower containment with a limited calorimeter thickness. However, this type of detector sees a reduction in precision due to the amount of energy lost in the absorbing material. The fraction of energy observed is defined as the sampling fraction $f_{samp} = E_{active}/(E_{active} + E_{passive})$ and it is used to quantify the energy loss. The knowledge of the sampling fraction of a calorimeter allows to rescale the measured energy to account for the unobserved contribution. The actual energy resolution of a realistic calorimeter is deteriorated by different contributions and can be written in a general way as [42]:

$$\frac{\sigma}{E} = \frac{a}{\sqrt{E}} \oplus \frac{b}{E} \oplus c \tag{2.5}$$

where the symbol '$\oplus$' indicates a quadratic sum, E is in considered in GeV, a is the sampling term, b the noise term, and c the constant term accounting for local non-uniformities in the response of the calorimeter.

2.2.4 The Muon Spectrometer

The Muon Spectrometer (MS) forms the outer part of the ATLAS detector and it is designed as to detect charged particles exiting the calorimeters in the range $|\eta| < 2.7$. The only particles that reach the MS are the muons, that are highly penetrating and release only a small fraction of their energy in the calorimeter system, due to their large mass and their long lifetime. Hence, the MS has a central role in the triggering of these particles in the pseudo-rapidity range $|\eta| < 2.4$. The layout of the muon spectrometer is shown in Figure 2.7.

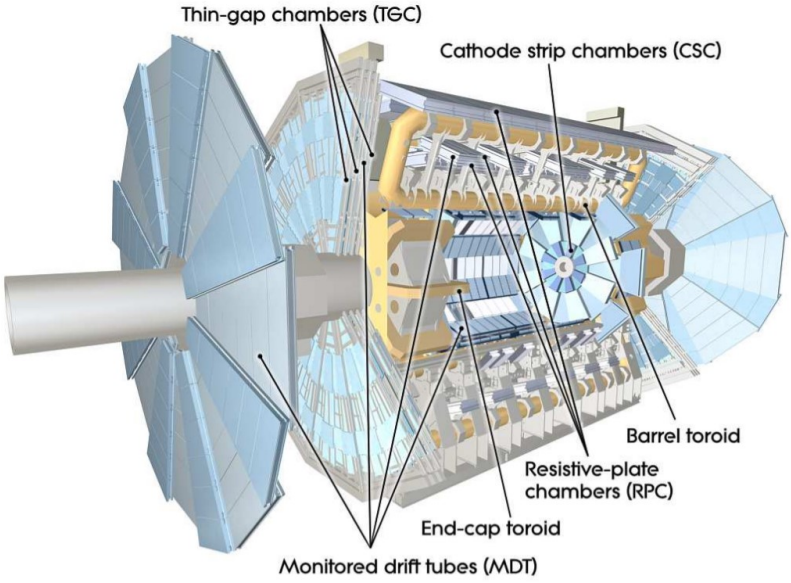

Figure 2.7: Cut-away view of the ATLAS muon system

The MS is based on the magnetic deflection of muon tracks in the large superconducting air-core toroid magnets, instrumented with separate trigger and high-precision tracking chambers. The magnetic field is designed to be mostly orthogonal to the muon direction, minimizing the scattering that would lead to a degradation of resolution. In the barrel region, tracks are measured in chambers arranged in three cylindrical layers around the beam axis; in the transition and end-cap regions, the chambers are installed in three layers in planes perpendicular to the beam. The MS is composed by different sub-detectors:

- The Monitored Drift Tubes (MDTs) provide precise measurements of the track coordinates in the principal bending direction of the magnetic field, over most of the pseudo-rapidity range. The maximum time to collect charge in the MDTs is 700ns which is why these detectors are suitable for precise measurements but too slow to be used as triggers.

- The Cathode Strip Chambers (CSCs) are located in the first layer of the endcap, in the pseudo-rapidity range $2.0 < |\eta| < 2.7$. They consist of multiwire proportional chambers with cathodes segmented into strips, that have a smaller maximum collection time to withstand the demanding rate and background conditions.

- The Resistive Plate Chambers (RPCs) and Thin Gap Chambers (TGCs) are the fast muon detectors, providing a signal within 15-25 ns. They supply the input to the trigger system in the pseudo-rapidity range $|\eta| < 2.4$. The RPCs are used in the barrel region and the TGCs in the end-cap regions. The trigger chambers serve

three purposes: providing bunch-crossing identification, providing well-defined p_T thresholds, and measuring the muon coordinates in the direction orthogonal to that determined by the MDT.

The MS momentum resolution is 2–3% at 10–100 GeV/c and 10% at 1 TeV, but the spectrometer can measure muon momenta with adequate momentum resolution and excellent charge identification in the range between ∼3 GeV and ∼3 TeV as well.

2.2.5 The Trigger and Data Acquisition System

The ATLAS TDAQ (Trigger and Data Acquisition) system is responsible for online processing, selecting and storing events of interest for the offline analysis. Events are selected using a two-stage trigger system, composed by: Level-1 (L1) and High-Level Trigger (HLT) steps [43].
The Level-1 trigger (L1) is an hardware-based system that uses custom electronics to trigger on reduced-granularity information from the calorimeter and muon detectors. This information is used to define regions of interest (RoI) in the detector and to perform an initial selection on the events. The L1 calorimeter trigger uses data both from the HC and EC to quickly reconstruct leptons, jets and missing transverse energy, employing simplified techniques if compared to the full offline reconstruction. The L1 muon trigger combines information from TGCs and RPCs to determine the deviation of the hit pattern from that of a muon with infinite momentum.
The information from the L1 trigger is directly passed to the software-based HLT. The complex set of algorithms of the HLT analyses the information from the RoI and the full event, applying a reconstruction similar to the offline one in a process time of ≈200 ms. These algorithms are executed on a computing farm, composed by 40000 selection applications, called Processing Units (PUs).
Once the event passes the L1 and HLT, the Sub-Farm Output (SFO) sends the data to permanent storage for offline reconstruction and exports the data to the Tier-0 facility at CERN computing centre.

2.2.6 The Luminosity Detectors

The integrated luminosity correlates the cross-section of a certain process with the observed number of events, therefore it has a crucial role in all measurements performed at ATLAS. ATLAS is equipped with a number of detectors dedicated to the measuring of luminosity: LUCID (LUminosity Cherenkov Integrating Detector), BCM (Beam Conditions Monitor), and, farther away from the IP, ALFA (Absolute Luminosity For ATLAS) and ZDC (Zero Degree Calorimeter).
LUCID is a Cherenkov detector formed by two identical sections, each one composed by 16 aluminium tubes f and placed at a distance of 17 m from the interaction point, around

the beam. The charged particles that enter these tubes emit a cone of Cherenkov light that is collected at the other end of the tube where photo-multipliers (PMTs) read out the signal. From the number of tubes with signal above threshold, the average number of interactions per bunch crossing can be evaluated and the instantaneous luminosity extracted.
The goal of the BCM [44] is to monitor instantaneous rates of collision and background and detect signs of beam instabilities, thus providing a luminosity measurement and beam monitoring at the same time. The virtue of this detector as a luminosity monitor is in its fast response of only 0.7 ns which allows for rejection of backgrounds from beam-halo.
ZDC and ALFA, located further away from the interaction point, are dedicated to the detection of forward neutrons in heavy-ion collisions and to total cross-section measurement, respectively.

Chapter 3

Top-pair production cross-section at LHC

Carrying out precise computations for Standard Model (SM) processes is fundamental for the prolific physics programme at the LHC. As experimental uncertainties are being pushed down to the percent level, thanks to the increasing amount of collected data, accurate predictions are a pressing necessity for many relevant processes, both for SM measurements and for new-physics searches, that rely on a precise modelling of the SM. The sensitivity to small deviations from the SM predictions, in particular, depends directly on the size of theoretical uncertainties. To obtain precise SM computations, QCD radiative corrections are to be included at the next-to-leading order (NLO), and when possible at the next-to-next-to-leading order (NNLO) as well. In particular, NNLO results have been achieved for processes involving the top-quark, like top-quark pair [45] and single top-quark [46] production.

The computational framework used to perform the calculations presented in this thesis is MATRIX (MUNICH Automates qT subtraction and Resummation to Integrate X-sections) [47], which features a parton-level Monte Carlo generator capable of computing fiducial cross sections and distributions for Higgs boson, vector-boson, vector-boson pair and top-pair production processes up to NNLO in QCD. All possible leptonic decay channels of the vector bosons are considered, and spin correlations and off-shell effects are included by accounting for all resonant and non-resonant diagrams, thereby allowing to apply realistic fiducial cuts on the phase-space of the respective leptonic final state [48].

The calculation of the processes at NNLO is highly demanding in terms of CPU resources and it requires a high level of parallelisation as well as the use of multi-core high-performance computing (HPC). The MATRIX program handles the splitting of the calculation in parallel jobs according to the number of threads available in the machine. In particular, the calculations used for this work, and presented hereinafter, have been performed on two multi-core machines: theophys02, kindly granted by the theory

group of INFN Bologna and the Department of Physics and Astronomy of the University of Bologna; HPC cluster 'MATRIX', an infrastructure of the Open Physics Hub (https://site.unibo.it/openphysicshub/en/infrastructures/the-hub) of the Department of Physics and Astronomy of the University of Bologna.

3.1 The MATRIX program

The computation of a QCD cross section at NNLO requires the evaluation of tree-level contributions with up to two additional unresolved partons, of one-loop contributions with one unresolved parton and of purely virtual contributions. Due to the presence of infrared (IR) divergences at intermediate stages of the calculation, the implementation of the corresponding scattering amplitudes in a complete NNLO calculation is a highly non-trivial task. In particular, a straightforward combination of the real and virtual contributions is not possible since the divergences affect these components in different ways. MATRIX achieves NNLO accuracy by using a process independent implementation of the transverse-momentum (qT) subtraction formalism in combination with a fully automated implementation of the Catani–Seymour dipole subtraction method [49] within the Monte Carlo program MUNICH [50].
The qT-subtraction formalism is a method used to handle and cancel IR divergences in NLO and NNLO computations. This method is based on the fact that the qT distribution has a process-independent structure at small qT, that is explicitly known up to NNLO through the formalism of transverse-momentum resummation [51], for the production of a colourless final-state system. With this information, the dependence of the cross section on the qT can be completely determined for small qT and a process-independent, although non-local, IR subtraction counter-term can be constructed for this entire class of processes. In the qT-subtraction method, the cross section for a generic process $pp \to F + X$, where F is a colourless system, can be written up to (N)NLO as [48]

$$d\sigma^{F}_{(N)NLO} = \mathcal{H}^{F}_{(N)NLO} \otimes d\sigma^{F}_{LO} + \left[d\sigma^{F+jets}_{(N)LO} - d\sigma^{CT}_{(N)NLO} \right]. \tag{3.1}$$

The term $\mathrm{d}\sigma^{F+jet}_{(N)LO}$ represents the cross section for the production of the system F+jet at (N)LO accuracy. If Eq. 3.1 is applied at NNLO, the NLO cross section $\mathrm{d}\sigma^{F+jet}_{NLO}$ is finite, provided that $qT \neq 0$, but it diverges in the limit $qT \to 0$. The process-independent counter-term $\mathrm{d}\sigma^{CT}_{(N)NLO}$ guarantees the cancellation of this divergence (its general expression is provided in [51]).
The universal structure of the NLO and NNLO hard-collinear coefficients $\mathcal{H}^{F}_{NLO}$ [52] and $\mathcal{H}^{F}_{NNLO}$ [53] has been obtained, respectively, from the one-loop corrections and from the results for Higgs and vector-boson production in terms of the suitably subtracted two-loop corrections to the respective Born subprocesses.

At NNLO QCD, MATRIX provides a process library for computing colour-singlet processes. The Monte Carlo program MUNICH, which is capable of computing both QCD and EW corrections to any SM process at NLO accuracy, constitutes the core of the MATRIX system. MUNICH contains a general implementation of an extremely efficient, multi-channel based phase-space integration, and employs an automated implementation of the Catani–Seymour dipole-subtraction method for massless [54] and massive [55] partons. All tree-level and one-loop amplitudes are obtained from OpenLoops [56], through an automated interface. Thanks to this functionality inherited from MUNICH, in principle MATRIX is able to immediately perform any SM calculation up to NLO accuracy.
In order to promote MUNICH to a Monte Carlo integrator at NNLO QCD, the F+jet cross section at NLO ($\mathrm{d}\sigma^{F+jet}_{NLO}$) is combined with a process-independent implementation of the qT-subtraction formalism for both gg- and $q\bar{q}$-initiated processes within the MATRIX framework. The universal nature of the counter-term $\mathrm{d}\sigma^{CT}_{(N)NLO}$ and the hard-collinear coefficients $\mathcal{H}^{F}_{NNLO}$ in Eq. 3.1 allows MATRIX to perform NNLO QCD computations for the hadro-production of any set of colourless final-state particles, as long as the corresponding two-loop virtual amplitudes for the Born-level subprocesses are available. As the remaining process-dependent ingredients are available in MUNICH+OpenLoops and the implementation of the qT-subtraction formalism is fully universal, any new colour singlet production process can be added to the MATRIX library by implementing the necessary two-loop amplitudes.
Further information about how the divergences of the terms in the square bracket of Eq. 3.1 are handled through the introducion of a technical cut-off r_{cut} on the dimensionless quantity $r = qT/M$ (with M representing the invariant mass of the colourless system) thus rendering both terms separately finite, can be found in [48].

3.2 Higher order corrections and scale uncertainties

Higher order diagrams (NLO, see Figure 3.1, and NNLO) need to be considered when comparing theoretical predictions to data in $t\bar{t}$ production, as they contribute significantly to the total production cross-section ($\sigma_{t\bar{t}}$). This is due to the large number of diagrams involved in the calculations as well as to the perturbative expansion coefficient α_S $\sim$O(0.1), that is sufficiently large to make the contribution of such diagrams non-negligible.
When the NNLO QCD correction is included, $\sigma_{t\bar{t}}$ can be predicted with an accuracy of about 5% [57]. This total uncertainty is the result of the contributions of a number of sources, the most important ones being higher order terms (beyond NNLO) that are not considered, PDF uncertainties and parametric m_t and α_S uncertainties. It is important to note that these sources of uncertainty are all comparable in magnitude, which indicates how challenging it would be to obtain a further reduction in the error of top-quark

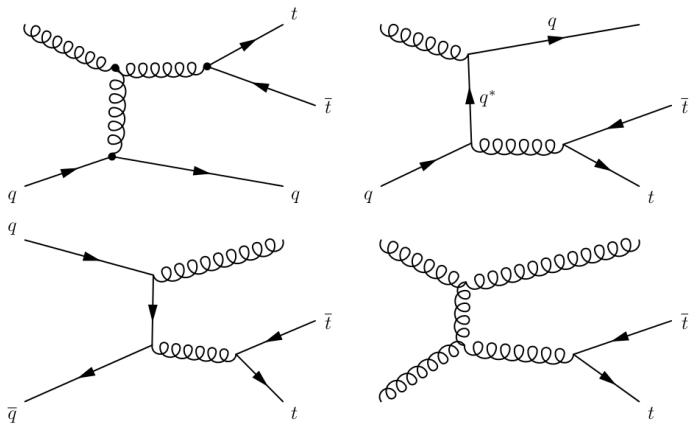

Figure 3.1: Example of some $t\bar{t}$ production diagrams at NLO.

pair production at the LHC, even in the long run. The following level of contributions to the uncertainty of σ_{tot} are of about 1% and include EW corrections, finite top-quark width and various non-perturbative effects. The sources of uncertainty in $t\bar{t}$ differential distributions can be predicted using this uncertainty breakdown for σ_{tot} as an indicator, however, these sources can vary wildly in different kinematic regions.
To account for missing higher order terms, we consider as a proxy the variation of factorisation and renormalisation scales. As a prerequisite to scale variation, one needs to specify a default central scale μ_0, that is chosen based on the criterion of perturbative convergence, accounting for LO, NLO and NNLO corrections. We assume that the nominal scale μ_0 that we are seeking is the same for both the renormalisation and factorisation scales, i.e. $\mu_{R,0}= \mu_{F,0}= \mu_0$. Scale variation, however, is done independently for μ_F and μ_R:

$$\mu_{F,R} \in (\frac{\mu_0}{2}, 2\mu_0) \qquad \text{with} \qquad 0.5 \leq \frac{\mu_R}{\mu_F} \leq 2, \tag{3.2}$$

and the cases where the two scale acquire the two opposite extreme values are not considered. The functional form used for the central scale is the one found to be optimal for $m_{t\bar{t}}$ in [57, 58]:

$$\mu_0 = \frac{H_T}{4} \qquad \text{where} \qquad H_T = \sqrt{m_t^2 + p_{T,t}^2} + \sqrt{m_t^2 + p_{T,\bar{t}}^2}, \tag{3.3}$$

where m_t and $p_{T,t/\bar{t}}$ are the mass and the average transverse momentum of the top or antitop-quark, respectively. Theoretical predictions of the measured quantities are required to be as precise as possible, in order to be quantitatively comparable with experimental measurements and thus allow us to extract physics parameters. Therefore, we compute the cross-sections for $t\bar{t}$ production at LO, NLO and NNLO accuracy to evaluate how higher order corrections impact the value and the uncertainty of the total

cross-section.
These calculations are performed with MATRIX, with a numerical precision of 0.5% for the total cross section, using the NNPDF31_lo_as_0118 [59], PDF4LHC15_nlo_100 and PDF4LHC15_nnlo_100 [60] PDF sets , for the following values of the top-quark mass:

$$m_t = \{168, 169, 170, 170.5, 171, 171.5, 172, 172.5, \\ 173, 173.5, 174, 174.5, 175, 176, 177\} \text{ GeV}. \tag{3.4}$$

The values of the inclusive $t\bar{t}$ cross-section computed for these values of m_t are shown in Figure 3.2. The points correspond to the data obtained for the central, nominal scale $\mu_R = \mu_F = \mu_0$, while the error bars refer to scale uncertainties, calculated as the difference between the values obtained for $\mu_R = \mu_F = \frac{\mu_0}{2}$ and the nominal value (upper bar) and between the nominal value and the ones for the scales $\mu_R = \mu_F = 2\mu_0$ (lower bar).

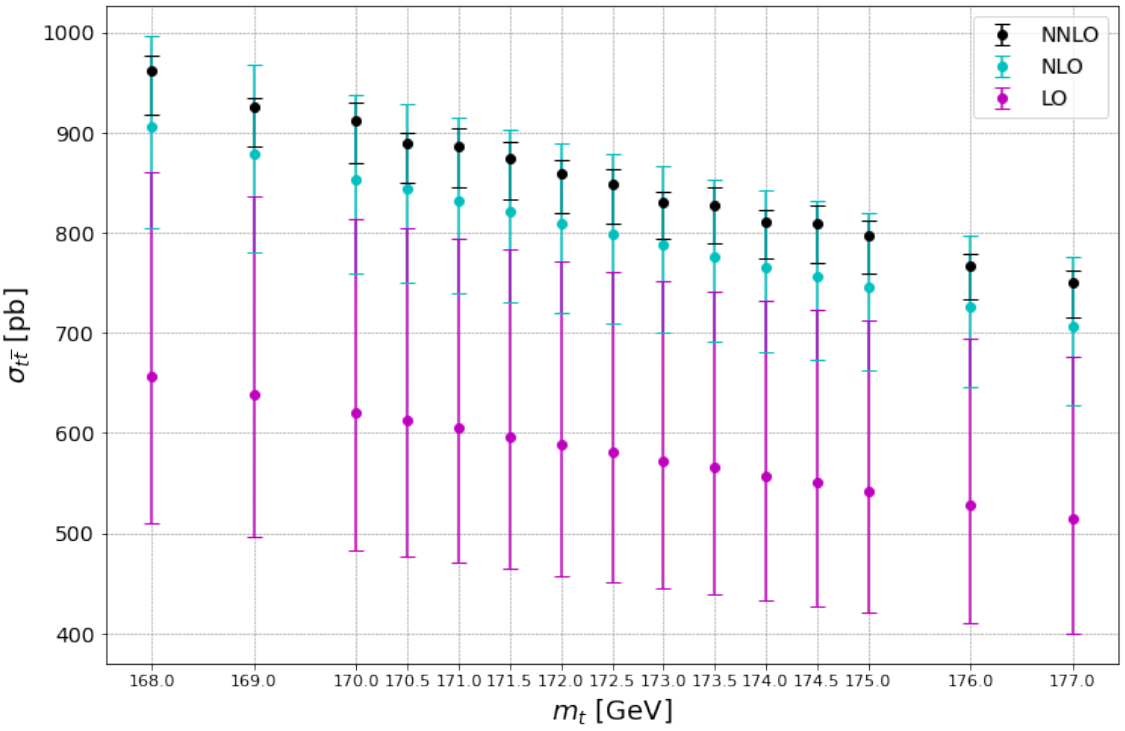

Figure 3.2: Plot showing the values of the total cross-section for $t\bar{t}$ production at LO (magenta), NLO (cyan) and NNLO (black) accuracy. The error bars for these three sets of values refer to scale uncertainties.

The inclusion of higher order corrections in the computation of $\sigma_{t\bar{t}}$ leads to higher values for the total production cross-section and to a clear reduction in scale uncertainties. The results obtained at LO accuracy are significantly lower than those produced at

NLO and NNLO accuracy, although comparable within uncertainties. This figure also shows the dependence of the prediction for the cross-section $\sigma_{t\bar{t}}$ on the top-quark pole mass, that can be parametrised as shown in [61], as a reduction in the uncertainties of the predictions leads to an increased sensitivity to the top-quark mass.

3.3 Differential distributions versus top-quark mass

Further information can be gathered considering the differential cross-section for top-pair production. The differential measurements we employ are those as a function of the invariant mass ($m_{t\bar{t}}$) and the average transverse momentum of the top or antitop-quark (p_T^t). The set of bins used in this thesis is the one utilised by ATLAS [62] for their measurements of these distributions (see Table 3.1), as it allows for an immediate comparison between theoretical predictions and the experimental results, which will be performed in Section 4.

Observable	Bin edges
p_T^t	{0, 50, 100, 160, 225, 300, 360, 475, 1000} GeV
$m_{t\bar{t}}$	{325, 400, 480, 580, 700, 860, 1020, 1250, 1500, 2000} GeV

Table 3.1: Bin edges used by ATLAS for measurements of p_T^t and $m_{t\bar{t}}$

The absolute cross-section $\sigma_{t\bar{t}}^i$ for each bin i of these distributions is calculated by MATRIX and it is then divided by the bin width W_i, in order to obtain the absolute differential cross-section as a function of the variable x, with x=p_T^t, $m_{t\bar{t}}$:

$$\left(\frac{d\sigma}{dx}\right)_i = \frac{\sigma_{t\bar{t}}^i}{W_i}. \tag{3.5}$$

The relative differential cross-section as a function of the kinematic parameter x is computed for each bin i as

$$\frac{1}{\sigma}\left(\frac{d\sigma}{dx}\right)_i = \frac{1}{W_i}\frac{\sigma_{t\bar{t}}^i}{\sum_j \sigma_{t\bar{t}}^j}. \tag{3.6}$$

The values obtained for the absolute and relative differential cross-section as functions of the top-quark pair mass $m_{t\bar{t}}$ are shown in Figure 3.3 and 3.4, while those of the absolute and relative differential cross-section as functions of p_T^t are in Figure 3.5 and 3.6, respectively.

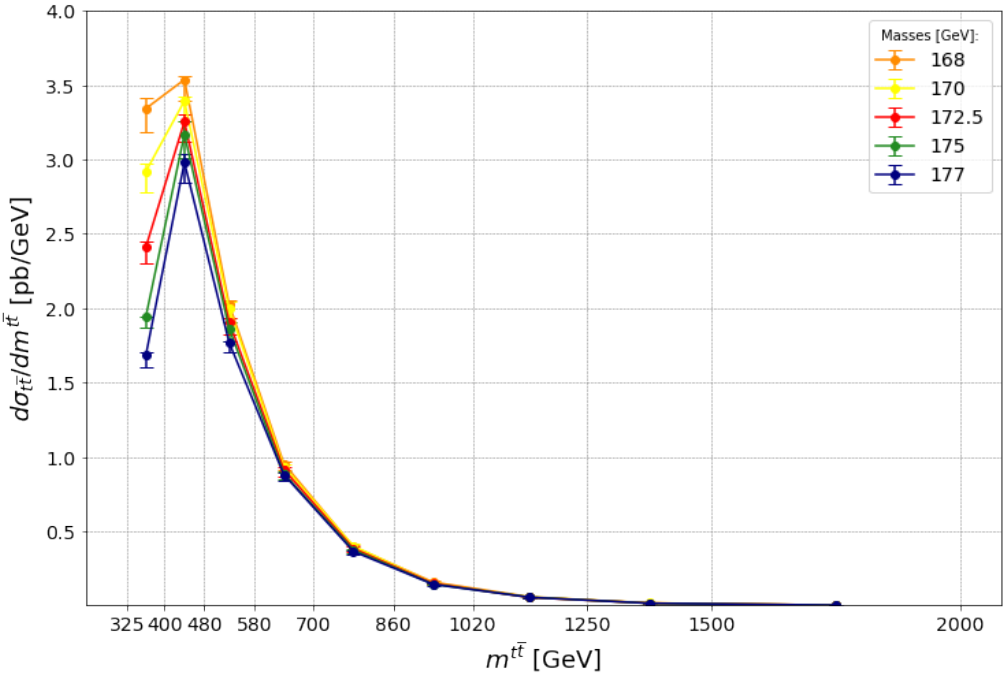

Figure 3.3: Plot showing the absolute differential cross-section as a function of $m_{t\bar{t}}$ for different input values of the top-quark mass.

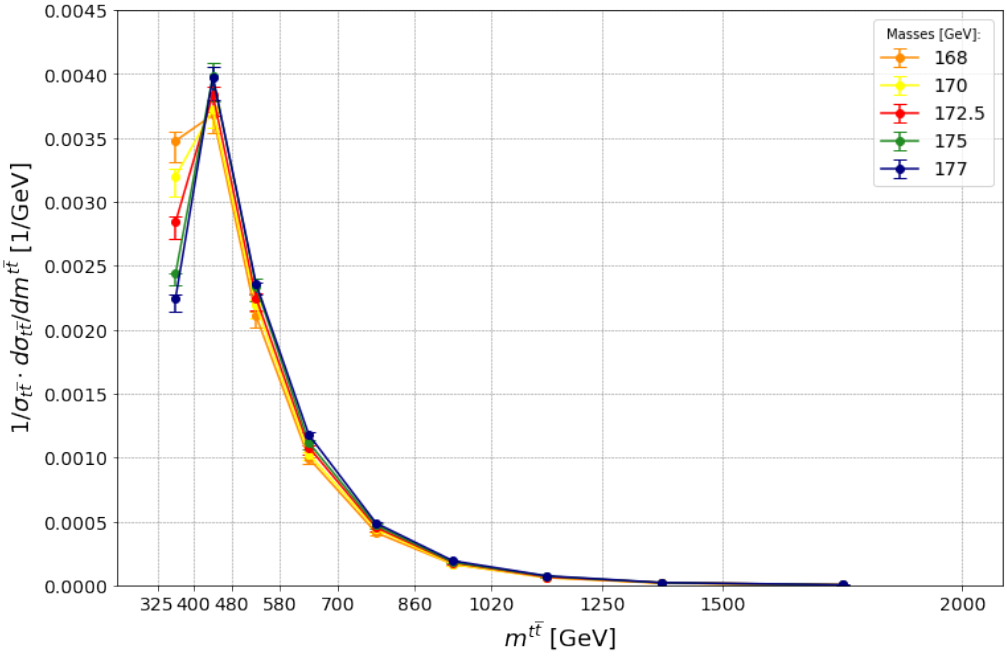

Figure 3.4: Plot showing the relative differential cross-section as a function of $m_{t\bar{t}}$ for different input values of the top-quark mass.

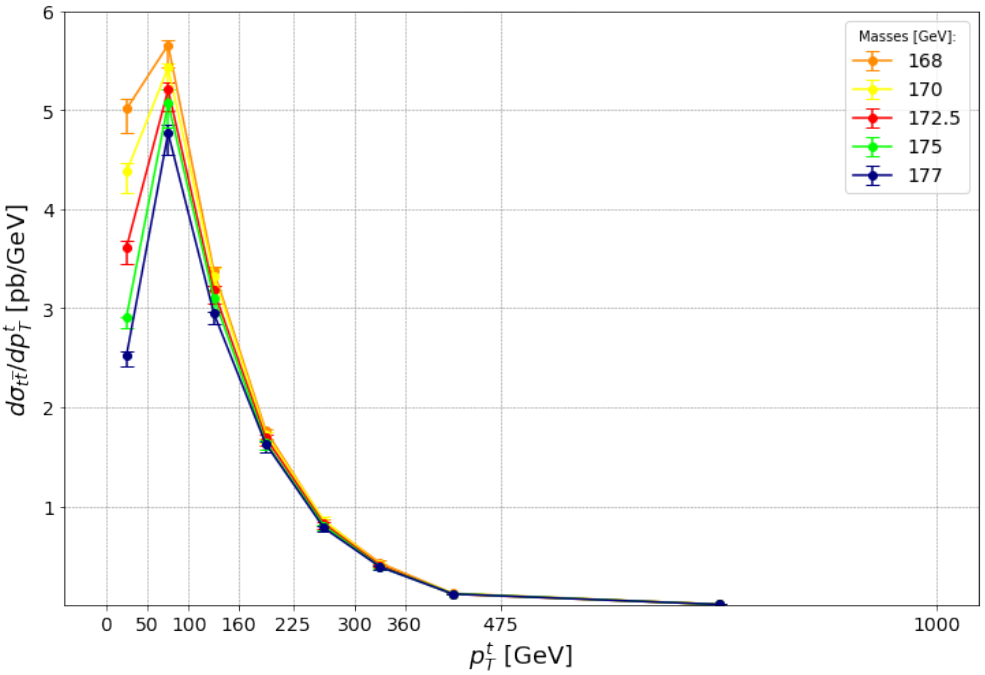

Figure 3.5: Plot showing the absolute differential cross-section as a function of p_T^t for different input values of the top-quark mass.

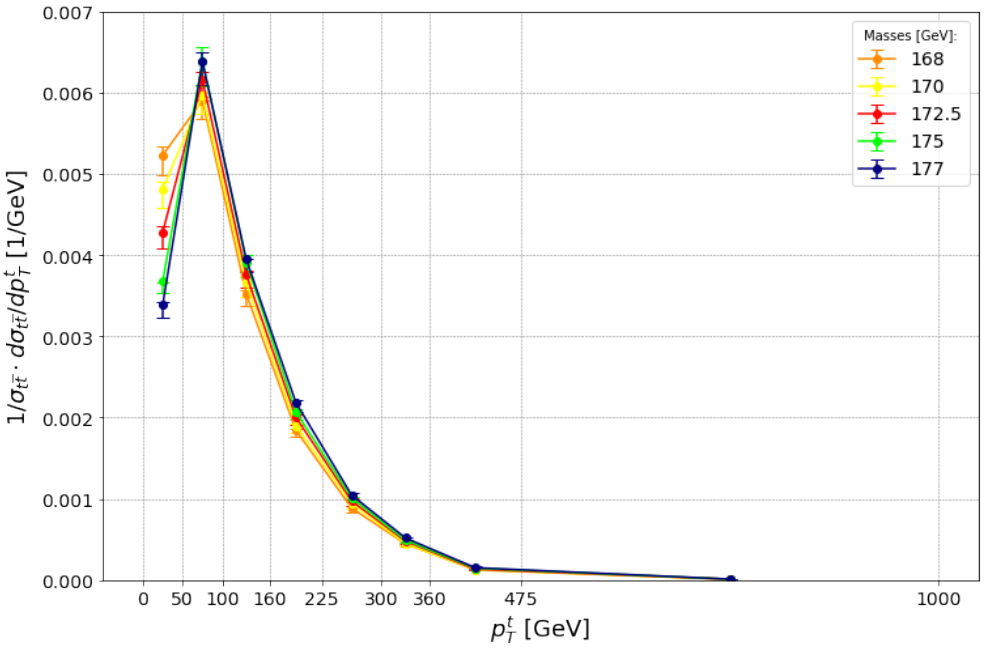

Figure 3.6: Plot showing the relative differential cross-section as a function of p_T^t for different input values of the top-quark mass.

These plots show the results for different values of the top-quark mass in order to assess the sensitivity of the different bins to m_t. The height of the error bars of each value of mass corresponds to the difference between the cross-section values obtained for the dynamic scales $\mu_R = \mu_F = \frac{\mu_0}{2}$ and $\mu_R = \mu_F = 2\mu_0$[1]. The most sensitive bins to changes in m_t are the lowest ones, in the ranges where the bulk of the cross section lies. In the tails, however, the sensitivity is dramatically reduced, which can be explained by the fact that in the tails the top-quark is effectively mass-less (the finite-mass effects are suppressed by powers of p_t^T or $m_{t\bar{t}}$) [63].

[1]In a few of the bins of some of the mass values employed, the maximum difference between the cross-section values obtained for the different scales corresponded to the scales $\mu_R = \mu_F = \frac{\mu_0}{2}$ and $\mu_R = \mu_F = \mu_0$. However, they constituted a very small minority and the difference with the scales $\mu_R = \mu_F = \frac{\mu_0}{2}$ and $\mu_R = \mu_F = 2\mu_0$ was diminutive, therefore the latter were employed in the whole analysis.

Chapter 4

Top mass measurement from ATLAS results

In this section the theoretical predictions generated with MATRIX are compared to experimental data collected at ATLAS for two different decay channels, in order to extract the top-quark mass. Two extractions are carried out: the first one is performed using a Bayesian approach considering the total production cross-section values; while the second is based on the minimisation of the reduced $\tilde{\chi}^2$ in the comparison of the predicted and the measured values for the absolute differential cross-section as a function of $m_{t\bar{t}}$. Further qualitative comparisons are drawn using both the absolute and relative differential cross-sections.

4.1 Total cross-section for top-quark pair production

The predictions for the total top-quark pair ($t\bar{t}$) production cross-section are compared to the inclusive cross-section $\sigma_{t\bar{t}}$ measured in proton–proton collisions at $\sqrt{s} = 13$ TeV, via events with an opposite-charge $e\mu$ pair and b-tagged jets, using 36.1 fb^{-1} of data collected in 2015–16 by the ATLAS experiment at the LHC [61]. Both theoretical and experimental values are shown in Figure 4.1, and the intersection of these curves gives an unambiguous extraction of the top-quark pole mass.
This extraction is performed using Markov Chain Monte Carlo (MCMC) and a Bayesian approach [64], that are further discussed in Appendix A, for each of the seven scales obtained from the variation of the renormalisation and factorisation scales. The value of the top-quark mass obtained with this analysis is

$$m_t = 173.4^{+1.7}_{-2.5} \text{ GeV}, \tag{4.1}$$

where uncertainties are calculated as the envelope (see Figure 4.2) of the uncertainties obtained at different scales, given by the 68% credibility interval of the top-quark mass

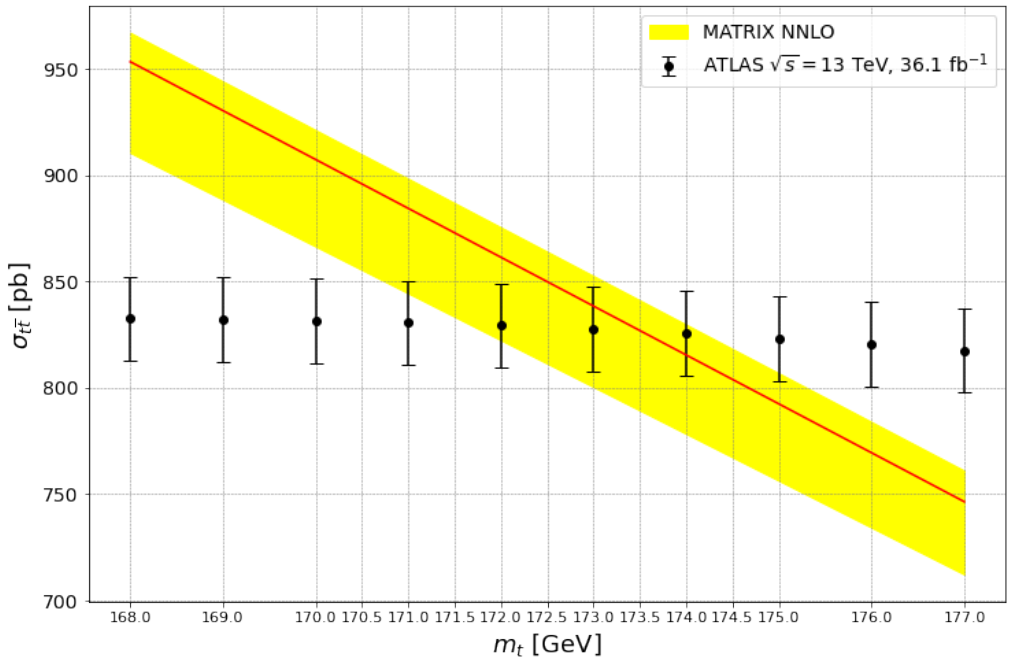

Figure 4.1: Predicted $t\bar{t}$ cross-section at $\sqrt{s} = 13$ TeV as a function of the top-quark pole mass m_t^{pole}. The yellow band indicates the scale uncertainties in the prediction, while the experimental measurements with their uncertainties are shown by the black points with error bars.

probability density function (pdf) obtained using the MCMC method. In Figure 4.3, the pdf for m_t at the nominal scale is shown, highlighting the uncertainty interval, which is chosen as the smallest interval containing the 68% of the pdf.

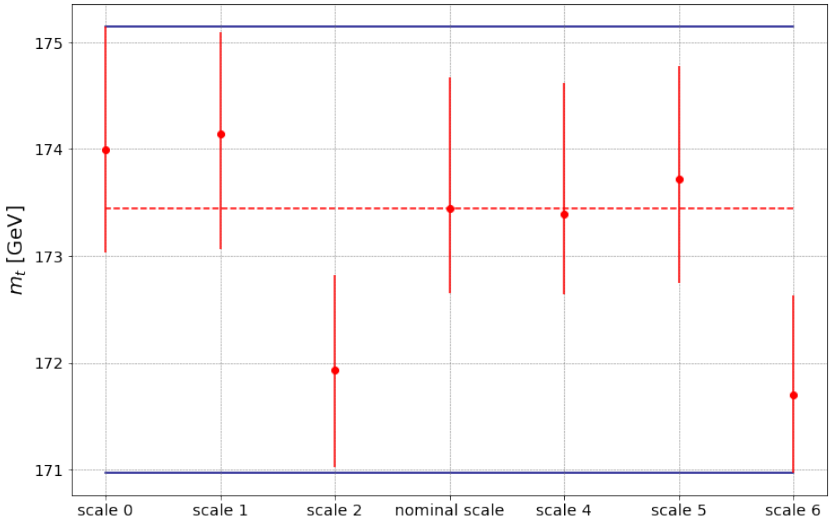

Figure 4.2: Extractions of the top-quark mass for the different energy scales (red markers), where the red bars represent the 68% credibility interval of the top-quark pdf. The envelope of the uncertainties is shown by the two blue horizontal lines, while the value of m_t of the central scale is highlighted by the red dashed line.

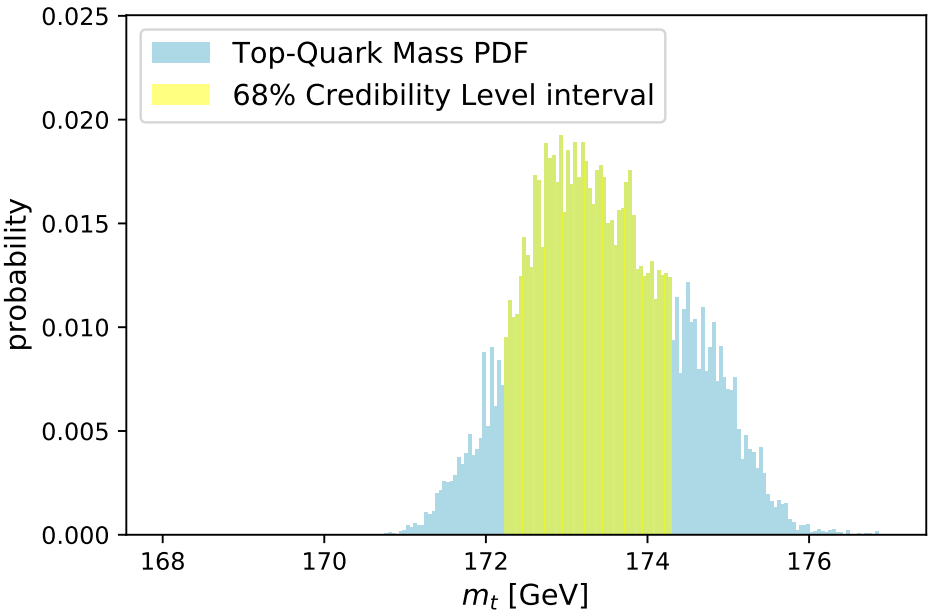

Figure 4.3: Plot showing the probability density distribution of the top-quark mass for the nominal energy scale.

This result is in good agreement with the one calculated in [61], that is $m_t = 173.1^{+2.0}_{-2.1}$ GeV, obtained using a different prediction for the differential cross-section [65] and including the PDF uncertainties as well. The result obtained her shows a more asymmetrical uncertainty, reflecting the symmetry induced by the chosen nominal scale $\frac{\hat{H}_T}{4}$.

4.2 Parton level differential cross-section results

QCD calculations at NNLO of the differential cross-section for the production of top-quark pairs are compared to differential cross-section measurements at parton level in the lepton + jets channel [62]. The results are presented as functions of two kinematic variables characterising the top-quark and $t\bar{t}$ system, p_T^t and $m_{t\bar{t}}$. The study is performed using data from pp collisions at centre-of-mass energy of 13 TeV collected in 2015 and 2016 by the ATLAS detector at the CERN Large Hadron Collider (LHC), corresponding to an integrated luminosity of 36 fb^{-1}.
Figure 4.4 presents the values of the absolute differential cross-section at parton level as a function of $m_{t\bar{t}}$ for a selection of values of the top-quark mass (m_t=$\{168, 170, 172.5, 175, 177\}$ GeV), while the corresponding relative distributions are shown in Figure 4.5. In Figure 4.6 and Figure 4.7, respectively, the absolute and relative differential cross-sections at parton level as functions of p_T^t are presented for the same set of top-quark mass values.

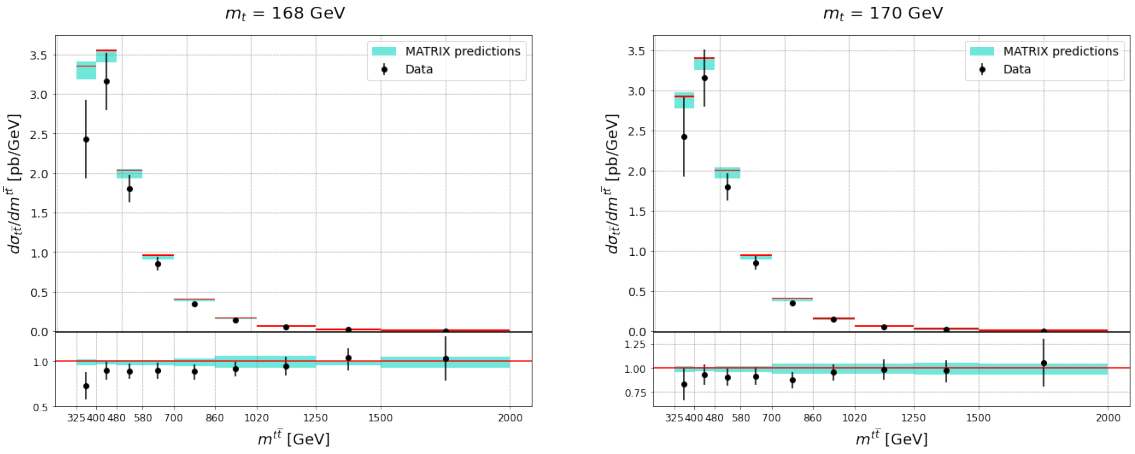

(a)

(b)

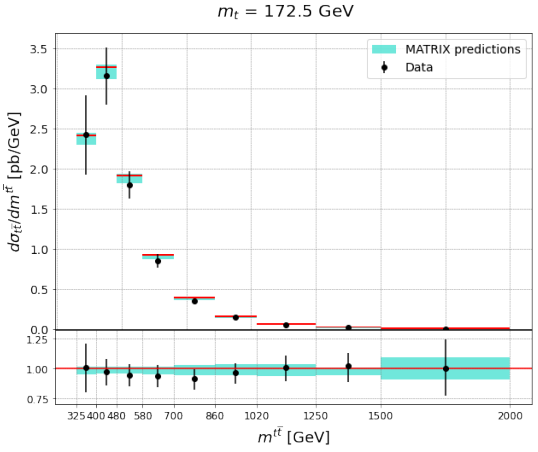

(c)

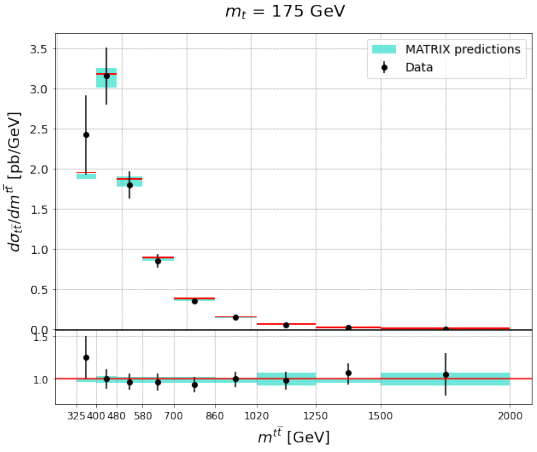

(d)

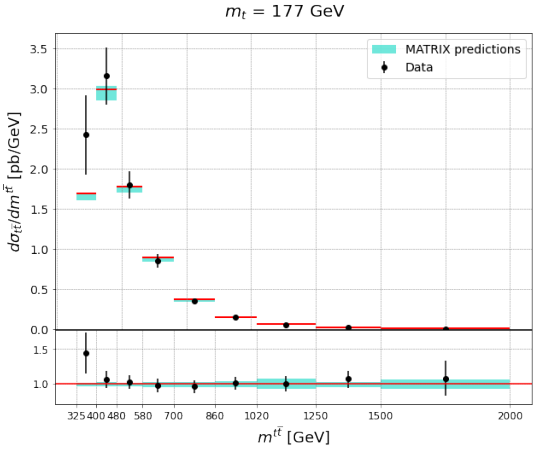

(e)

Figure 4.4: Absolute differential cross-sections as functions of $m_{t\bar{t}}$ at parton level, for five values of the top-quark mass.

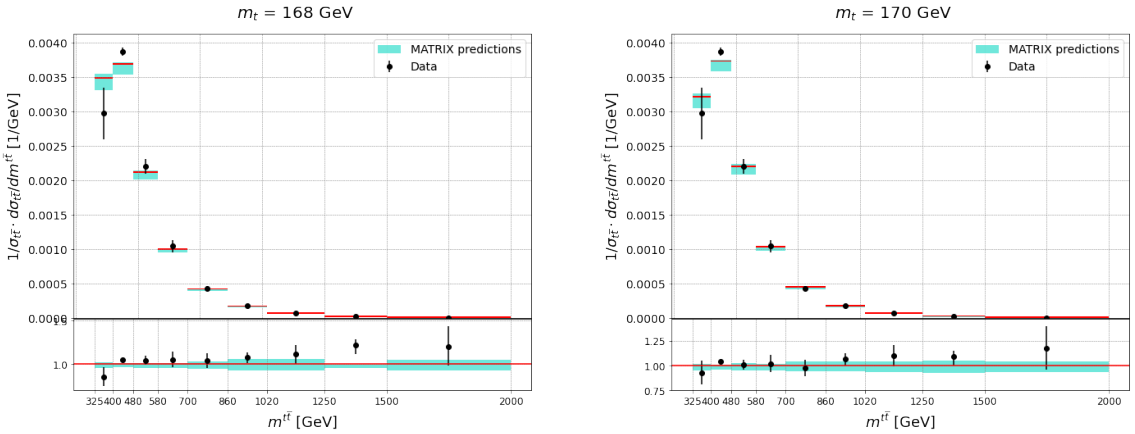

(a)

(b)

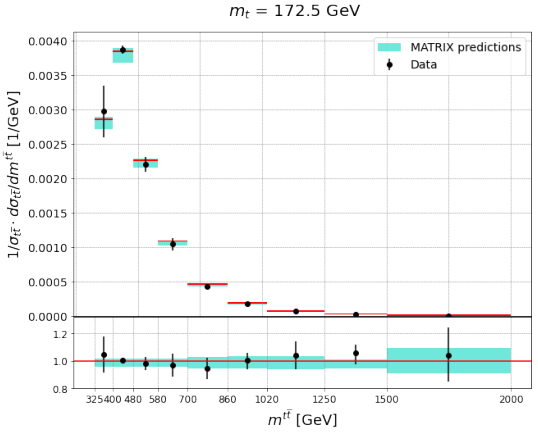

(c)

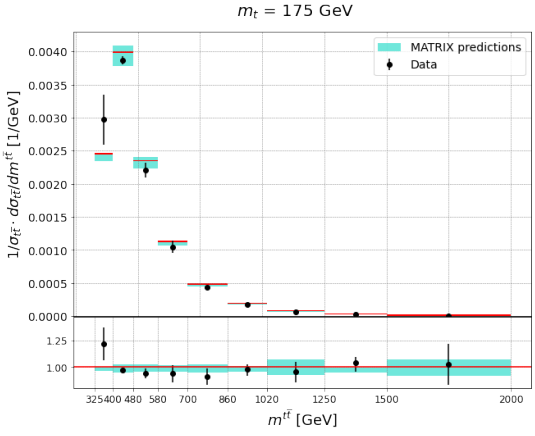

(d)

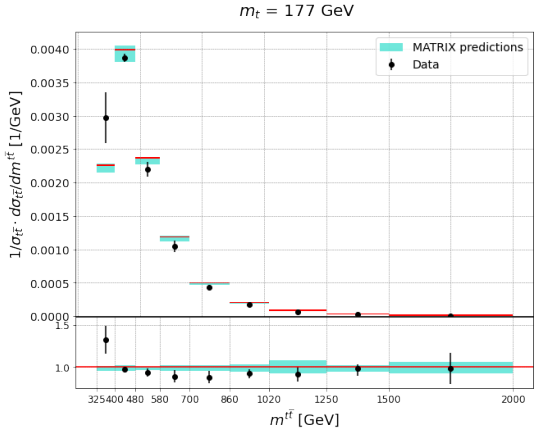

(e)

Figure 4.5: Relative differential cross-sections as functions of $m_{t\bar{t}}$ at parton level, for five values of the top-quark mass.

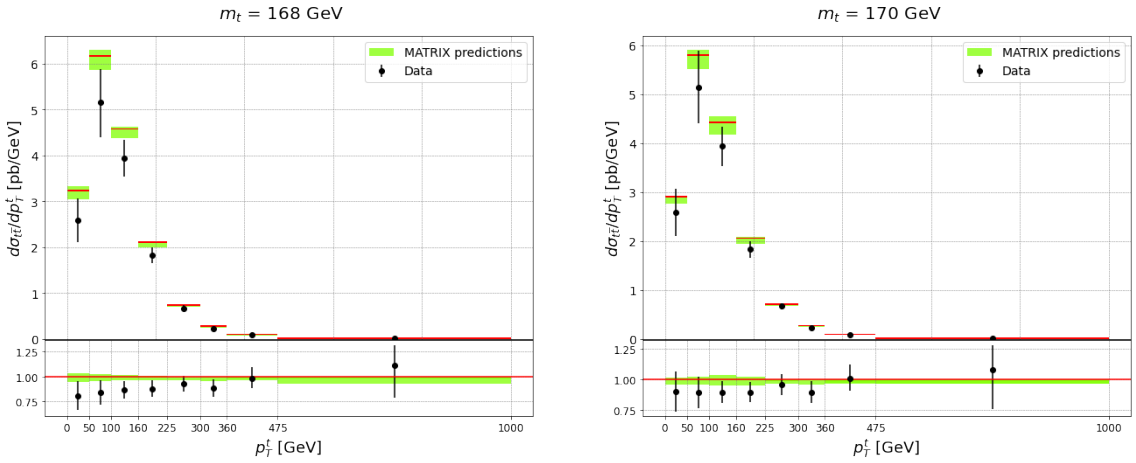

(a)

(b)

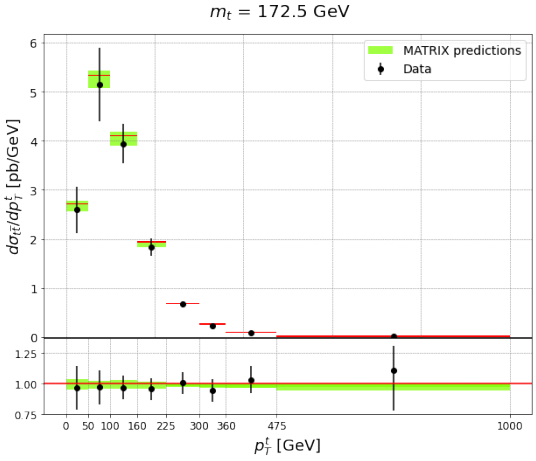

(c)

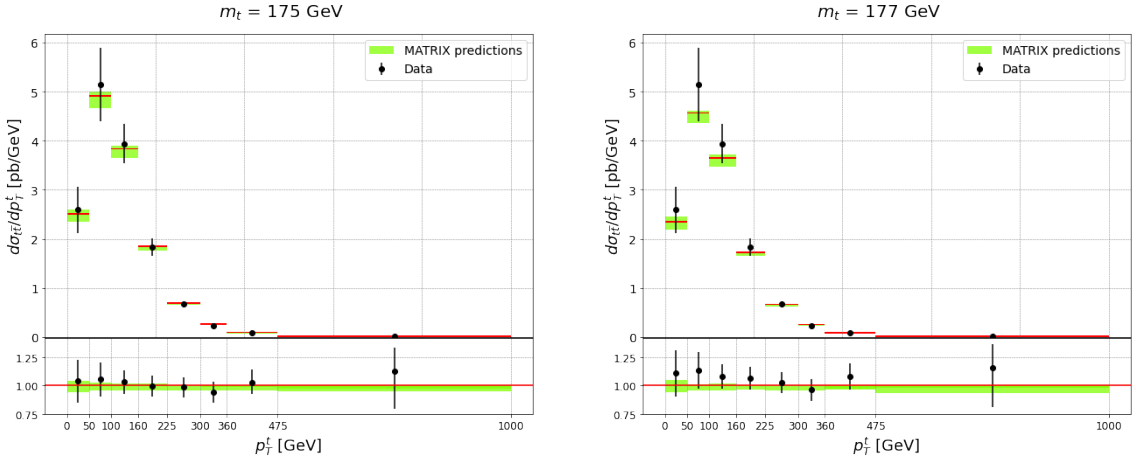

(d)

(e)

Figure 4.6: Absolute differential cross-sections as functions of p_T^t at parton level, for five values of the top-quark mass.

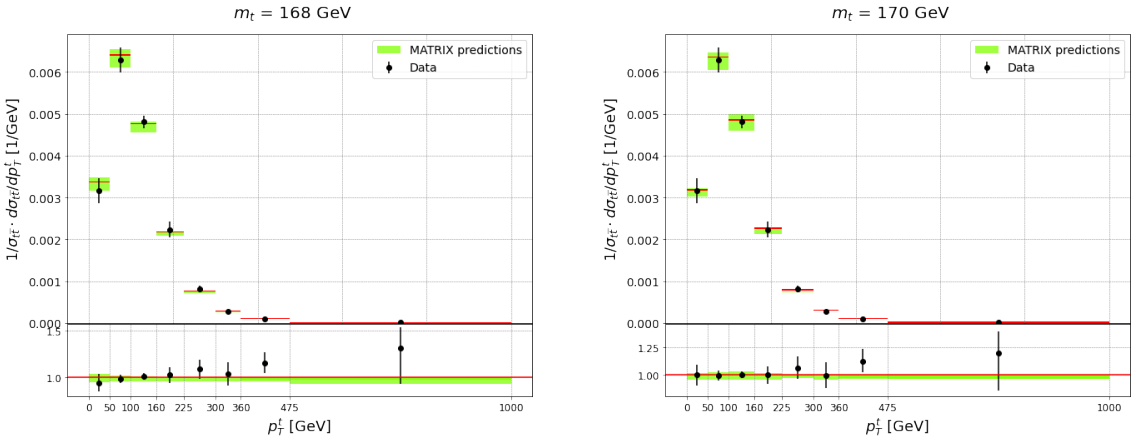

(a)

(b)

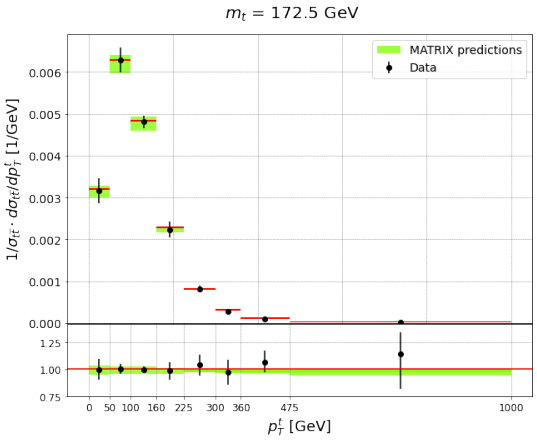

(c)

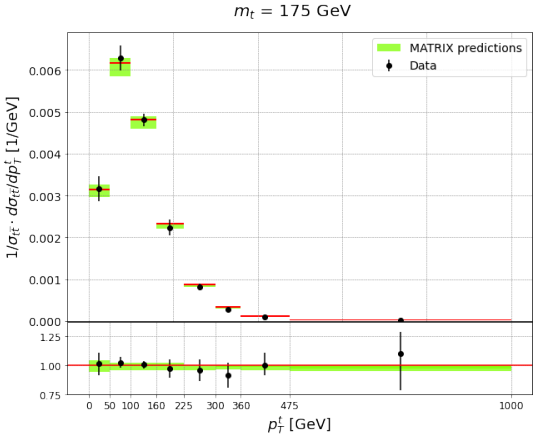

(d)

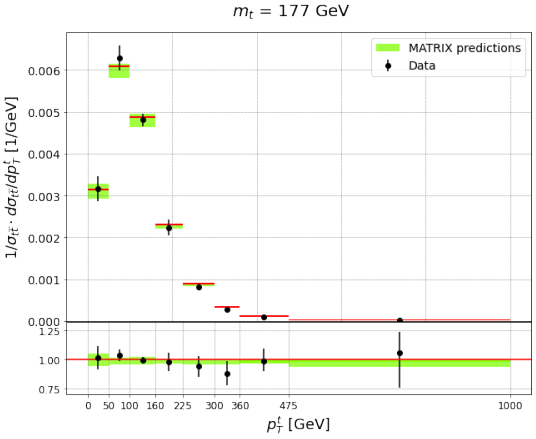

(e)

Figure 4.7: Relative differential cross-sections as functions of p_T^t at parton level, for five values of the top-quark mass.

In the lower part of these plots the ratio of the values from measured data to the ones from the predictions ($\frac{\text{measured values}}{\text{predicted values}}$) is shown in order to present a clearer comparison, especially for the highest bins. The red line refers to the differential cross-section values at the nominal energy scale of the theoretical predictions, while the black markers represent the measured data. The uncertainties of the experimental data are obtained by propagating the individual uncertainties to the measured cross-sections [62], while the uncertainties of predictions obtained with MATRIX are given by scale uncertainties (blue and green bands).
It can be noted, by comparing the plots in Figures 4.4 and 4.5 to those in Figures 4.6 and 4.7, that the distribution in $m_{t\bar{t}}$ is more sensitive to the top-quark mass, which is the reason behind the choice of using this distribution alone in the extraction of m_t.

4.2.1 Top-quark mass extraction through $\tilde{\chi}^2$ evaluation

A quantitative comparison between the predictions and the measured absolute differential cross-section as a function of the invariant $t\bar{t}$ mass is performed by means of a reduced $\tilde{\chi}^2$ calculation. The $\tilde{\chi}^2$ is evaluated using the full covariance matrix COV_{N_b} [62], accounting for the statistical and systematic uncertainties, and following the equation:

$$\tilde{\chi}^2 = \frac{1}{N_b} \cdot V_{N_b}^T \cdot COV_{N_b}^{-1} \cdot V_{N_b} \tag{4.2}$$

where V_{N_b} is the vector of residuals, i.e. the vector of differences between the measured and predicted cross-sections, and $N_b = 9$ is the number of degrees of freedom, which corresponds the number of bins employed as the distribution under examination is an absolute one. Before inversion, the uncertainties on theoretical predictions are added to the diagonal terms of the covariance matrix of the experimental data.
For each of the values of the top-quark mass reported in Eq. 3.4, the $\tilde{\chi}^2$ is calculated as shown in Eq. 4.2 for all possible combinations of scale variation. Subsequently a second degree polynomial fit is performed on the (m_t, $\tilde{\chi}^2$) pairs in order to find a minimum of the $\tilde{\chi}^2$ distribution ($\tilde{\chi}^2_{min}$) and extract the corresponding value of the top-quark mass. The value for m_t obtained with this analysis is

$$m_t = 172.9^{+3.0}_{-2.9} \text{ GeV}. \tag{4.3}$$

The uncertainties are obtained as the envelope of the uncertainties at different dynamic scales, that are calculated by finding the intersections of the polynomial fit with a horizontal line at $\tilde{\chi}^2_{min}$+1 (shown in Figure 4.8) and subtracting from the corresponding two values of mass the one obtained for the minimum. It is important to note that the value of m_t extracted from the differential distribution presents higher uncertainties than the one obtained from the total cross-section (Eq. 4.4). This is due to the fact that the systematic uncertainties in the the lepton+jets channel, particularly those of the b-tagging, are much larger than those in the dilepton channel.

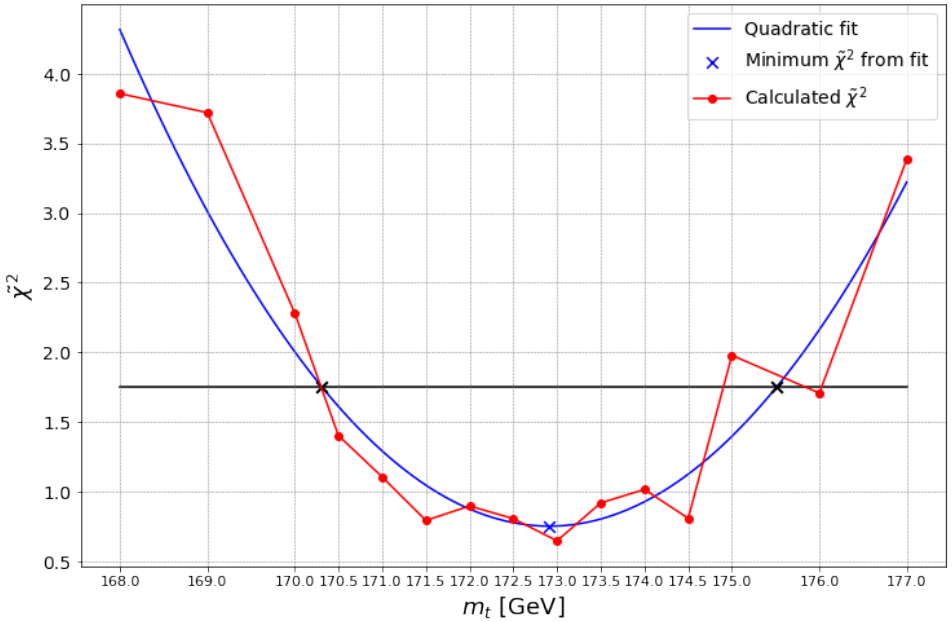

Figure 4.8: Plot showing the $\tilde{\chi}^2$ values for the different top-mass values (red markers) for the nominal energy scale. The quadratic fit and its minimum are shown in blue, while the horizontal line at $\tilde{\chi}^2_{min}+1$ and the intersection with the fit curve are in black.

Conclusions

There are several reasons that motivate an accurate study of the top-quark and of its mass. For instance, it is a way to verify the consistency of the EW theory through higher-order corrections to the W-boson mass. A highly precise value of the top-quark mass could also be of aid in the enquiry on the stability of the SM vacuum.
However, the impossibility of observing isolated quarks turns any possible definition of quark mass into a purely theoretical construction. When considering the pole mass of the quark, i.e. the QCD equivalent of the definition of mass in QED, the perturbative series shows rather poor convergence even at low orders of perturbation, which results in the need of truncating it. This leads to an uncertainty in the value of the quark pole mass of the order of Λ_{QCD}. Different definitions of the mass parameter can be employed, depending on the characteristic scale of the physical process studied, and the most advantageous one can be used in the expression of theoretical predictions. An extraction of the top-quark mass in a well-defined renormalization scheme can be carried out considering the production cross section.
In this work, two extractions of the top-quark mass m_t are presented using NNLO theory predictions and measurements of both the top-quark pair production cross-section and differential distributions. The theoretical calculations have been performed by the program MATRIX, executed utilising two multi-core machines: theophys02, granted by the theory group of INFN Bologna and the Department of Physics and Astronomy of the University of Bologna; and the HPC cluster 'MATRIX' of the Open Physics Hub (https://site.unibo.it/openphysicshub/en/infrastructures/the-hub) of the Department of Physics and Astronomy of the University of Bologna.
By comparing these predictions of the total $t\bar{t}$ production cross-section with the cross-section measured in proton-proton collisions at $\sqrt{s}$=13 TeV, considering events with an opposite-charge $e\mu$ pair and b-tagged jets and using 36.1 fb^1 of data collected in 2015-16 by the ATLAS experiment at the LHC, the extracted value of the top-quark mass is

$$m_t = 173.4^{+1.7}_{-2.5} \text{ GeV}. \tag{4.4}$$

The comparison was performed using a Bayesian approach and Markov Chain Monte Carlo.
A second value of m_t was extracted considering the measurements of the differential

cross-section as a function of the invariant mass $m_{t\bar{t}}$ in the lepton + jets channel, using data from pp collisions at centre-of-mass energy of 13 TeV collected in 2015 and 2016 by the ATLAS detector, corresponding to an integrated luminosity of 36 fb^1. The value of the top-quark mass obtained through a minimisation of the reduced $\tilde{\chi}^2$ between predicted and measured data is

$$m_t = 172.9^{+3.0}_{-2.9} \text{ GeV}. \tag{4.5}$$

The value of m_t obtained with the differential distribution is affected by higher uncertainties than the one extracted from the total cross-section, a fact that can be attributed to the higher systematic uncertainties in the lepton+jets channel rather than in the dilepton channel, especially those ascribable to the b-tagging.

Appendix A

Mass extraction from data and predictions using Markov Chain Monte Carlo and a Bayesian approach

A.1 Bayesian inference

Bayesian inference is a statistical inference method that uses Bayes' theorem to evaluate the background knowledge by analysing the sample data and to collect new data to improve the prior understanding. In Bayesian inference, the posterior probability is derived as a consequence of two antecedents: a prior probability, i.e. the distribution of the parameters before any data is observed ($\pi(\theta)$), and a likelihood function ($L(D|\theta)$), i.e. the distribution of the observed data conditional on its parameters. Bayesian theory can be used to determine the posterior distribution ($\pi(\theta|D)$) of the parameter vector θ, given the knowledge of the data D [64, 66]:

$$\pi(\theta|D) = \frac{L(D|\theta) \cdot \pi(\theta)}{\int L(D|\theta) \cdot \pi(\theta) d\theta}, \tag{A.1}$$

where the denominator is the marginal distribution of the data set.
Therefore, the calculation of the posterior distribution revolves around three functions: the likelihood function, the prior distribution, and the marginal distribution. When data from experimental measurements is available, all relevant measured information is already included in the likelihood function when making statistical inference to θ. In the selection of a prior distribution $\pi(\theta)$, one needs to consider both the measured data and available prior knowledge: if the prior distribution is obtained from the existing data and research results, it is called a data-based prior distribution, while the term

non-data-based prior distribution refers to a prior distribution resulting from subjective judgement or theory.
The denominator of Eq. A.1, that is the marginal distribution, is a constant related only to the data set and independent from the parameters, and its solution can rarely be obtained analytically. Markov Chain Monte Carlo (MCMC) methods can be used in order to avoid a direct calculation of the marginal distribution in a Bayesian approach.

A.2 MCMC and the Metropolis-Hastings algorithm

A Markov chain is a stochastic model that describes a sequence of possible events in which the probability of each event is solely determined by the state obtained in the previous event. Markov processes are the foundation for Markov Chain Monte Carlo, a class of general stochastic modeling methods that are used for simulating sampling from complex probability distributions.
The MCMC approach can be implemented using a variety of algorithms, resulting in various Markov chains. Among them, the Metropolis–Hastings (M–H) algorithm [67, 68] is one of the most commonly used methods, constructing a Markov Chain with an invariant target distribution. In order to estimate this target distribution, the M–H algorithm needs an auxiliary probability density function (pdf) $q(x, y)$, generally called proposal function or proposal distribution. As the proposal function needs to be independent of the distribution that is to be sampled, its shape is a fundamental factor in its choice. The M-H algorithm can be illustrated as the following steps [66, 69]:

(i) Set an arbitrary starting point θ_0 for calculation at $i = 0$;

(ii) Generate a new value θ_* from the proposal function $q(x, y)$;

(iii) Calculate the probability of acceptance

$$\rho = \min \left[\frac{q(\theta_i|\theta_*)\pi(\theta_*|D)}{q(\theta_*|\theta_i)\pi(\theta_i|D)}, 1 \right]; \tag{A.2}$$

(iv) Generate a random number u from an uniform distribution between [0,1];

(v) If $u < \rho$, then set $\theta_{i+1} = \theta_*$; otherwise set $\theta_{i+1} = \theta_i$ and $i = i + 1$, and return to Step (ii)

This transition preserves the stationary density $\pi(\theta|D)$ if the chain is irreducible, that is, if q has a wide enough support to eventually reach any region of the parameter space with positive mass under $\pi(\theta|D)$ [70]. For this reason, the most common choices in the selection of a proposal function are the Breit-Wigner and the normal distributions.

A.3 Top-quark mass extraction

In order to extract the value of the top-quark mass from the comparison of the predictions obtained with MATRIX with the experimental data from [61], the Metropolis-Hastings algorithm is carried out for five different Markov Chains, with randomly chosen starting points, for each combination of the factorisation and renormalisation scales.
The prior distribution employed in this work is considered to be flat and, since multiplicative factors in the likelihood function do not affect the results, there is no need to include it in the calculations. A logarithmic function is used as the likelihood function, while a normal distribution is employed for the proposal distribution, with standard deviations of 1 GeV and 5 pb for the two parameters, m_t and $\sigma_{t\bar{t}}$, respectively.
Figure A.1 shows thow the different chains explore the parameter space, for the values obtained at the nominal scale ($\mu_R = \mu_F = \mu_0$). Starting from very different positions in the parameter space, all the chains quickly converge and sample the same distribution. The pdf of the parameter of interest, m_t, is then obtained from the 2D distribution integrating out $\sigma_{t\bar{t}}$, a method called "marginalisation".

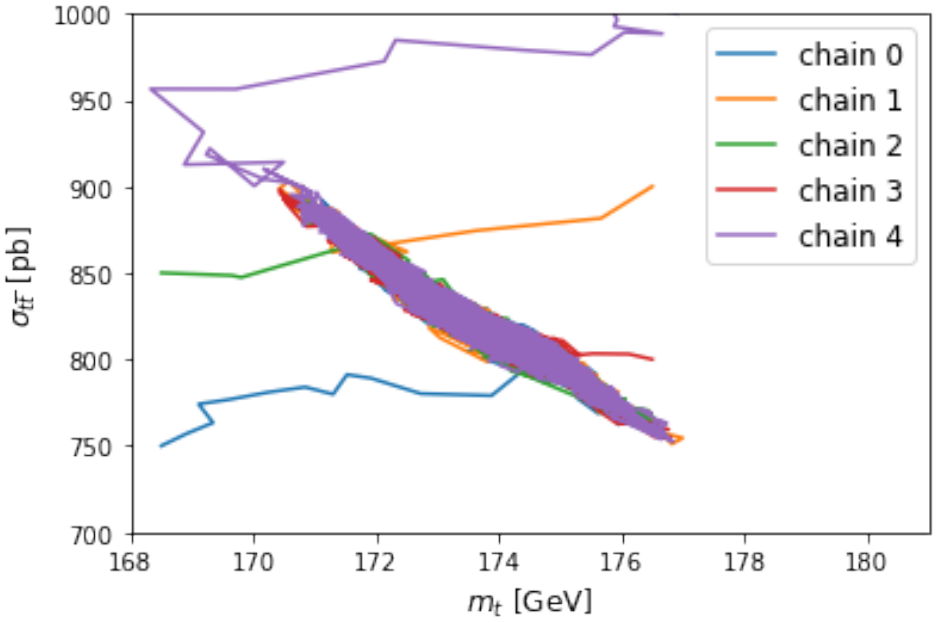

Figure A.1: Plot of the five Markov chains used in the extraction of the top-quark mass at the nominal energy scale.

The mass and the uncertainty for the different energy scales are evaluated from the pdf by concatenating the different chains and removing the first 2000 points, as they are considered to be part of the warm-up phase, in which the sequences get closer to the

mass of the distribution. Figure A.2 presents the pdfs for the five distinct chains, in order to show that each of the Markov processes converges to the same distribution.

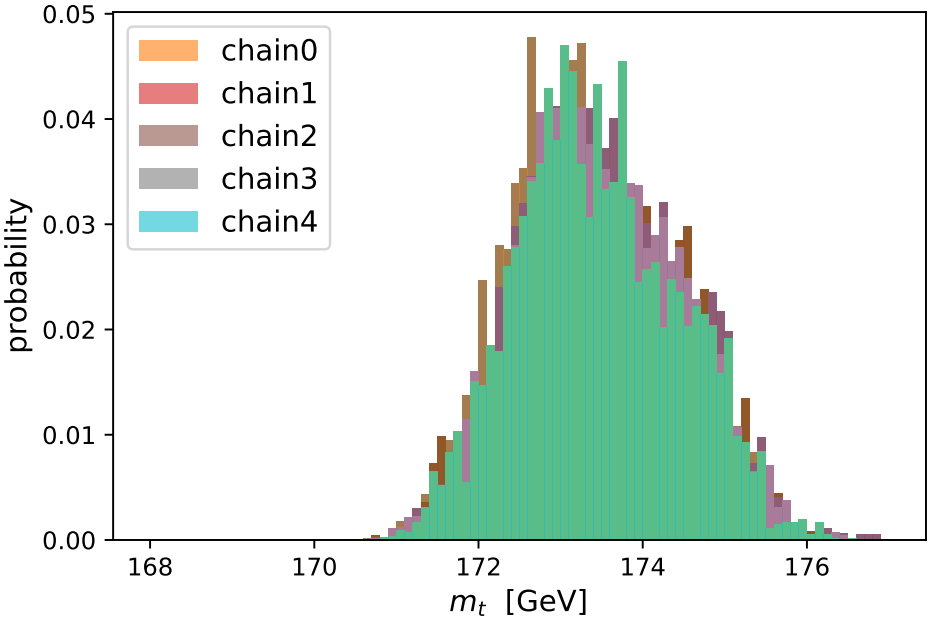

Figure A.2: Plot showing the probability density distributions of top-quark mass of each of the five Markov chains, for the nominal energy scale.

Bibliography

[1] P. A. M. Dirac and R. H. Fowler. The quantum theory of the electron. *Proceedings of the Royal Society of London. Series A, Containing Papers of a Mathematical and Physical Character*, 117(778):610–624, 1928.

[2] S. Braibant, G. Giacomelli, and M. Spurio. *Particles and fundamental interactions: an introduction to particle physics*. Dordrecht, 2012. https://www.springer.com/gp/book/9789400724631. Editor Springer.

[3] K.A. Olive. Review of Particle Physics. *Chinese Physics C*, 40(10):100001, Oct 2016.

[4] N. Cabibbo. Unitary Symmetry and Leptonic Decays. *Phys. Rev. Lett.*, 10:531–533, Jun 1963. https://link.aps.org/doi/10.1103/PhysRevLett.10.531.

[5] M. Kobayashi and T. Maskawa. CP-Violation in the Renormalizable Theory of Weak Interaction. *Progress of Theoretical Physics*, 49(2):652–657, 02 1973.

[6] P. W. Higgs. Broken Symmetries and the Masses of Gauge Bosons. *Phys. Rev. Lett.*, 13:508–509, Oct 1964. https://link.aps.org/doi/10.1103/PhysRevLett.13.508.

[7] F. Englert and R. Brout. Broken Symmetry and the Mass of Gauge Vector Mesons. *Phys. Rev. Lett.*, 13:321–323, Aug 1964. https://link.aps.org/doi/10.1103/PhysRevLett.13.321.

[8] S. Weinberg. A Model of Leptons. *Phys. Rev. Lett.*, 19:1264–1266, Nov 1967. https://link.aps.org/doi/10.1103/PhysRevLett.19.1264.

[9] A. Salam. *Weak and electromagnetic interactions*, pages 244–254. https://www.worldscientific.com/doi/abs/10.1142/9789812795915_0034.

[10] G.'t Hooft. Renormalizable Lagrangians for massive Yang-Mills fields. *Nuclear Physics B*, 35(1):167–188, 1971. https://www.sciencedirect.com/science/article/pii/0550321371901398.

[11] ATLAS Collaboration. Observation of a new particle in the search for the Standard Model Higgs boson with the ATLAS detector at the LHC. *Physics Letters B*, 716(1):1–29, 2012. https://www.sciencedirect.com/science/article/pii/S037026931200857X.

[12] CMS Collaboration. Observation of a new boson at a mass of 125 GeV with the CMS experiment at the LHC. *Physics Letters B*, 716(1):30–61, 2012. https://www.sciencedirect.com/science/article/pii/S0370269312008581.

[13] M. Gell-Mann. A schematic model of baryons and mesons. *Physics Letters*, 8(3):214–215, 1964. https://www.sciencedirect.com/science/article/pii/S0031916364920013.

[14] G Zweig. An SU_3 model for strong interaction symmetry and its breaking; Version 2. page 80 p, Feb 1964. https://cds.cern.ch/record/570209. Version 1 is CERN preprint 8182/TH.401, Jan. 17, 1964.

[15] CDF Collaboration. Observation of Top Quark Production in $\overline{p}p$ Collisions with the Collider Detector at Fermilab. *Phys. Rev. Lett.*, 74:2626–2631, Apr 1995. https://link.aps.org/doi/10.1103/PhysRevLett.74.2626.

[16] D0 Collaboration. Observation of the Top Quark. *Phys. Rev. Lett.*, 74:2632–2637, Apr 1995. https://link.aps.org/doi/10.1103/PhysRevLett.74.2632.

[17] M. L. Perl, G. S. Abrams, A. M. Boyarski, et al. Evidence for anomalous lepton production in $e^+ - e^-$ annihilation. *Phys. Rev. Lett.*, 35:1489–1492, Dec 1975. https://link.aps.org/doi/10.1103/PhysRevLett.35.1489.

[18] S. W. Herb, D. C. Hom, L. M. Lederman, et al. Observation of a Dimuon Resonance at 9.5 GeV in 400-GeV Proton-Nucleus Collisions. *Phys. Rev. Lett.*, 39:252–255, Aug 1977. https://link.aps.org/doi/10.1103/PhysRevLett.39.252.

[19] W. R. Innes, J. A. Appel, B. C. Brown, et al. Observation of Structure in the Υ Region. *Phys. Rev. Lett.*, 39:1240–1242, Nov 1977. https://link.aps.org/doi/10.1103/PhysRevLett.39.1240.

[20] K. Ueno, B. C. Brown, C. N. Brown, et al. Evidence for the Υ'' and a Search for New Narrow Resonances. *Phys. Rev. Lett.*, 42:486–489, Feb 1979. https://link.aps.org/doi/10.1103/PhysRevLett.42.486.

[21] M. C. Smith and S. S. Willenbrock. Top-quark pole mass. *Phys. Rev. Lett.*, 79:3825–3828, Nov 1997. https://link.aps.org/doi/10.1103/PhysRevLett.79.3825.

[22] J. Erler and M. Schott. Electroweak precision tests of the Standard Model after the discovery of the Higgs boson. *Progress in Particle and Nuclear Physics*, 106:68–119, May 2019. http://dx.doi.org/10.1016/j.ppnp.2019.02.007.

[23] G. Corcella. The Top-Quark Mass: Challenges in Definition and Determination. *Frontiers in Physics*, 7:54, 2019. https://www.frontiersin.org/article/10.3389/fphy.2019.00054.

[24] S. Jindariani. Measurements of top quark properties in top pair production and decay at the LHC using the CMS detector. *Nuclear and Particle Physics Proceedings*, 273-275:2299–2306, 2016. 37th International Conference on High Energy Physics (ICHEP). https://www.sciencedirect.com/science/article/pii/S2405601415008640.

[25] Top quark mass summary plots Spring 2021. Technical report, CERN, Geneva, May 2021. All figures including auxiliary figures are available at https://atlas.web.cern.ch/Atlas/GROUPS/PHYSICS/PUBNOTES/ATL-PHYS-PUB-2021-015.

[26] ATLAS Collaboration. Measurement of the top quark mass with the template method in the $t\bar{t} \rightarrow$ lepton + jets channel using atlas data. *The European Physical Journal C*, 72(6), Jun 2012. http://dx.doi.org/10.1140/epjc/s10052-012-2046-6.

[27] F. Fiedler, A. Grohsjean, P. Haefner, and P. Schieferdecker. The matrix element method and its application to measurements of the top quark mass. *Nuclear Instruments and Methods in Physics Research Section A: Accelerators, Spectrometers, Detectors and Associated Equipment*, 624(1):203–218, Dec 2010. http://dx.doi.org/10.1016/j.nima.2010.09.024.

[28] V. M. Abazov et al. (D0 Collaboration). Measurement of the top quark mass in the lepton+jets channel using the ideogram method. *Physical Review D*, 75(9), May 2007. http://dx.doi.org/10.1103/PhysRevD.75.092001.

[29] F. Schilling. Top quark physics at the LHC: A review of the first two years. *International Journal of Modern Physics A*, 27(17):1230016, Jun 2012. http://dx.doi.org/10.1142/S0217751X12300165.

[30] The ATLAS, CDF, CMS, and D0 Collaborations. First combination of Tevatron and LHC measurements of the top-quark mass, 2014. arXiv: hep-ex/1403.4427.

[31] G. Degrassi. The role of the top quark in the stability of the SM Higgs potential, 2014. arXiv: hep-ph/1403.4427.

[32] D. Buttazzo, G. Degrassi, et al. Investigating the near-criticality of the Higgs boson. *Journal of High Energy Physics*, 2013(12), Dec 2013. http://dx.doi.org/10.1007/JHEP12(2013)089.

[33] V. Branchina, E. Messina, and A. Platania. Top mass determination, Higgs inflation, and vacuum stability. *Journal of High Energy Physics*, 2014(9), Sep 2014. http://dx.doi.org/10.1007/JHEP09(2014)182.

[34] ALICE Collaboration. The ALICE experiment at the CERN LHC. *Journal of Instrumentation*, 3(08):S08002–S08002, aug 2008. https://doi.org/10.1088/1748-0221/3/08/s08002.

[35] LHCb Collaboration. The LHCb detector at the LHC. *Journal of Instrumentation*, 3(08):S08005–S08005, aug 2008. https://doi.org/10.1088/1748-0221/3/08/s08005.

[36] CMS collaboration. The CMS experiment at the CERN LHC. *Journal of Instrumentation*, 3, August 2008. https://doi.org/10.1088/1748-0221/3/08/S08004.

[37] ATLAS Collaboration. The ATLAS experiment at the CERN large hadron collider. *Journal of Instrumentation*, 3(08):S08003–S08003, aug 2008. https://doi.org/10.1088/1748-0221/3/08/s08003.

[38] LHC Machine. *JINST*, 3:S08001, 2008. https://doi.org/10.1088/1748-0221/3/08/S08001.

[39] J. Wenninger. Approaching the Nominal Performance at the LHC. In *Proc. of International Particle Accelerator Conference (IPAC'17), Copenhagen, Denmark, 14â19 May, 2017*, number 8 in International Particle Accelerator Conference, pages 13–18, Geneva, Switzerland, May 2017. JACoW. https://doi.org/10.18429/JACoW-IPAC2017-MOYAA1.

[40] ATLAS Collaboration. ATLAS data quality operations and performance for 2015-2018 data-taking. *JINST*, 15:P04003. 43 p, Nov 2019. https://cds.cern.ch/record/2700249.

[41] E. Stanecka. The ATLAS Inner Detector operation, data quality and tracking performance, 2013. arXiv: hphysics.ins-det/1303.3630.

[42] C. W. Fabjan and F. Gianotti. Calorimetry for Particle Physics. *Rev. Mod. Phys.*, 75:1243–1286. 96 p, Oct 2003. https://cds.cern.ch/record/692252.

[43] ATLAS collaboration. Operation of the ATLAS trigger system in run 2. *Journal of Instrumentation*, 15(10):P10004–P10004, Oct 2020.

[44] H. Pernegger. First test results of a high-speed beam conditions monitor for the ATLAS experiment. *IEEE Transactions on Nuclear Science*, 52(5):1590–1594, 2005.

[45] ATLAS Collaboration. Measurement of the $t\bar{t}$ production cross-section in the lepton+jets channel at $\sqrt{s} = 13\,\text{TeV}$ with the ATLAS experiment. *Physics Letters B*, 810:135797, Nov 2020. http://dx.doi.org/10.1016/j.physletb.2020.135797.

[46] J. Campbell, T. Neumann, and Z. Sullivan. Single-top-quark production in the t-channel at NNLO. *Journal of High Energy Physics*, 2021(2), Feb 2021. http://dx.doi.org/10.1007/JHEP02(2021)040.

[47] MATRIX. MATRIX is available for download from: http://matrix.hepforge.org/.

[48] M. Grazzini, S. Kallweit, and M. Wiesemann. Fully differential NNLO computations with MATRIX. *The European Physical Journal C*, 78(7), Jun 2018. http://dx.doi.org/10.1140/epjc/s10052-018-5771-7.

[49] S. Catani and M. H. Seymour. A general algorithm for calculating jet cross sections in NLO QCD. *Nuclear Physics B*, 485(1-2):291–419, Feb 1997. http://dx.doi.org/10.1016/S0550-3213(96)00589-5.

[50] S. Kallweit, J. M. Lindert, P. Maierhöfer, S. Pozzorini, and M. Schönherr. NLO electroweak automation and precise predictions for w+multijet production at the LHC, 2015. arXiv: hep-PH/1412.5157.

[51] G. Bozzi, S. Catani, D. de Florian, and M. Grazzini. Transverse-momentum resummation and the spectrum of the higgs boson at the LHC. *Nuclear Physics B*, 737(1-2):73–120, Mar 2006. http://dx.doi.org/10.1016/j.nuclphysb.2005.12.022.

[52] D. de Florian and M. Grazzini. The structure of large logarithmic corrections at small transverse momentum in hadronic collisions. *Nuclear Physics B*, 616(1-2):247–285, Nov 2001. http://dx.doi.org/10.1016/S0550-3213(01)00460-6.

[53] S. Catani, L. Cieri, D. de Florian, G. Ferrera, and M. Grazzini. Universality of transverse-momentum resummation and hard factors at the NNLO. *Nuclear Physics B*, 881:414–443, Apr 2014. http://dx.doi.org/10.1016/j.nuclphysb.2014.02.011.

[54] S. Catani and M.H. Seymour. The dipole formalism for the calculation of QCD jet cross sections at next-to-leading order. *Physics Letters B*, 378(1-4):287–301, Jun 1996. http://dx.doi.org/10.1016/0370-2693(96)00425-X.

[55] S. Catani, S. Dittmaier, M. H. Seymour, and Z. Trócsányi. The dipole formalism for next-to-leading order QCD calculations with massive partons. *Nuclear Physics B*, 627(1-2):189–265, Apr 2002. http://dx.doi.org/10.1016/S0550-3213(02)00098-6.

[56] F. Cascioli, P. Maierhöfer, and S. Pozzorini. Scattering Amplitudes with Open Loops. *Physical Review Letters*, 108(11), Mar 2012. http://dx.doi.org/10.1103/PhysRevLett.108.111601.

[57] M. Czakon, D. Heymes, and A. Mitov. Dynamical scales for multi-tev top-pair production at the LHC. *Journal of High Energy Physics*, 2017(4), Apr 2017. http://dx.doi.org/10.1007/JHEP04(2017)071.

[58] D. Heymes. Differential distributions for top-quark pair production at NNLO. page 046, 10 2016. http://dx.doi.org/10.22323/1.260.0046.

[59] The NNPDF Collaboration. Parton distributions from high-precision collider data. *The European Physical Journal C*, 77(10), Oct 2017. http://dx.doi.org/10.1140/epjc/s10052-017-5199-5.

[60] S. Alekhin, S. Alioli, R. D. Ball, V. Bertone, et al. The PDF4LHC working group interim report, 2011. arXiv: hep-ph/1101.0536.

[61] ATLAS Collaboration. Measurement of the $t\bar{t}$ production cross-section and lepton differential distributions in $e\mu$ dilepton events from pp collisions at $\sqrt{s} = 13\,\text{TeV}$ with the atlas detector. *The European Physical Journal C*, 80(6), Jun 2020. http://dx.doi.org/10.1140/epjc/s10052-020-7907-9.

[62] Measurements of top-quark pair differential and double-differential cross-sections in the ℓ+jets channel with pp collisions at $\sqrt{s} = 13$ TeV using the ATLAS detector, 2019. https://doi.org/10.17182/hepdata.95758.

[63] A. M. Cooper-Sarkar, M. Czakon, M. A. Lim, A. Mitov, and A. S. Papanastasiou. Simultaneous extraction of α_s and m_t from LHC $t\bar{t}$ differential distributions, 2020. arXiv: hep-ph/2010.04171.

[64] A. Caldwell, D. Kollár, and K. Kröninger. BAT - The Bayesian analysis toolkit. *Computer Physics Communications*, 180(11):2197–2209, Nov 2009. http://dx.doi.org/10.1016/j.cpc.2009.06.026.

[65] M. Czakon and A. Mitov. Top++: A program for the calculation of the top-pair cross-section at hadron colliders. *Computer Physics Communications*, 185(11):2930–2938, Nov 2014. http://dx.doi.org/10.1016/j.cpc.2014.06.021.

[66] Hongrui Wang, Cheng Wang, Ying Wang, Xiong Gao, and Chen Yu. Bayesian forecasting and uncertainty quantifying of stream flows using Metropolis–Hastings Markov Chain Monte Carlo algorithm. *Journal of Hydrology*, 549:476–483, 2017. https://www.sciencedirect.com/science/article/pii/S0022169417302196.

[67] N. Metropolis, A. W. Rosenbluth, M. N. Rosenbluth, A. H. Teller, and E. Teller. Equation of State Calculations by Fast Computing Machines. *The Journal of Chemical Physics*, 21(6):1087–1092, 1953. https://doi.org/10.1063/1.1699114.

[68] W. K. Hastings. Monte Carlo sampling methods using Markov chains and their applications. *Biometrika*, 57(1):97–109, 04 1970. https://doi.org/10.1093/biomet/57.1.97.

[69] Mathematical Tools or Statistics, Monte Carlo, Group Theory. *Physics Letters B*, 667(1):316–339, 2008. Review of Particle Physics.https://www.sciencedirect.com/science/article/pii/S0370269308008551.

[70] C. P. Robert. The Metropolis-Hastings algorithm, 2016. arXiv: stat.CO/1504.01896.